An Investigation into the Discovery Potential for SUperSYmmetry at the LHC with Early Data from the ATLAS Detector

Paul Prichard

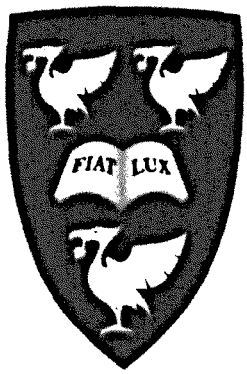

January 18, 2010

Abstract

To explain the large difference between the Planck scale and the electroweak scale, models in which there are super-symmetric partners of the particles in the Standard Model have been proposed. This thesis presents a study of analysis techniques which will optimise the discovery of such a model using Monte Carlo simulations of the ATLAS detector at CERN. The selections are based on features that differentiate SUper-SYmmetric (SUSY) events from Standard Model (SM) background processes. A study into a method for measuring the resolution of the missing transverse energy (E_T^{miss}) using data is performed. Finally an estimate of how much data will be needed to exclude or discover a set of benchmark mSugra SUSY points is presented.

Declaration

Acknowledgements

I would firstly like to thank STFC for their generous support throughout this thesis and without whom this work would not have been possible. I feel it is also important to mention Prof. Phil Allport, for giving me the opportunity to study at Liverpool. I would also like to thank my supervisors, Dr. Neil Jackson and Dr. Barry King for their insight into the world of physics and for their patience. Neil has kept me focused on the task at hand, and Barry has always been full of optimism, reassuring me that the goal is attainable. Dr. Steve Maxfield has also been a great help in the completion of this thesis, and at every stage has offered an unbiased point of view which has given me perspective, and his many stories have given me pause for thought.

Throughout the 4 years this PhD has taken, I have met many other weary travellers on the path toward the enlightenment that academic pursuit bestows. I would particularly like to thank Tina Potter for her company at many conferences and in Geneva, and mention must also go to Lily and Jessie Asquith for keeping me on the straight and narrow. Special thanks must go to Mark Tobin for lending me a CERN van when in desperate need, also Neil Thresher, AJ and Jason Lee for their friendships. I would like to thank my colleagues from Liverpool, both the HEP students and the nuclear students

and Mike Flowerdew has been a special help.

Finally, thanks must go to my parents and my brothers who have put up with all the niggling worries that a PhD entails. My education up to and including the PhD would not have been possible without their love and support.

Dedication

Dedicated to my parents .....

Contents

List of Figures

List of Tables

Chapter 1

Theory and Motivation

1.1 Introduction

Particle physics is the quest to understand the world around us at a fundamental level. The development of gauge theories (see section 1.2.2) led to the development of the Standard Model (SM) which took a huge leap in furthering our understanding. Whilst successful on many fronts, such as the correct predictions of the mass of the Z and W bosons, and existence of the top quark, there are problems with the SM. Examples are the lack of a mechanism for mass via the discovery of a Higgs boson, and the problem that neutrinos have mass. We now know that it is an incomplete theory. Extensions to the Standard Model, such as super-symmetric models, technicolour, or extra-dimensions may hold answers to some of the questions it raises. In this thesis the sensitivity to super-symmetry with data from ATLAS is investigated.

	Fermion Generation							
	1^{st}	2^{nd}	3^{rd}	Q	I	I_3	Y	$SU(3)_C$
Quarks	$\begin{pmatrix} u \\ d \end{pmatrix}_L$	$\begin{pmatrix} c \\ s \end{pmatrix}_L$	$\begin{pmatrix} t \\ b \end{pmatrix}_L$	$\begin{matrix} \frac{2}{3} \\ -\frac{1}{3} \end{matrix}$	$\begin{matrix} \frac{1}{2} \\ \frac{1}{2} \end{matrix}$	$\begin{matrix} \frac{1}{2} \\ -\frac{1}{2} \end{matrix}$	$\begin{matrix} \frac{1}{3} \\ \frac{1}{3} \end{matrix}$	$\begin{matrix} 3 \\ 3 \end{matrix}$
	$\begin{matrix} u_R \\ d_R \end{matrix}$	$\begin{matrix} c_R \\ s_R \end{matrix}$	$\begin{matrix} t_R \\ b_R \end{matrix}$	$\begin{matrix} \frac{2}{3} \\ -\frac{1}{3} \end{matrix}$	$\begin{matrix} 0 \\ 0 \end{matrix}$	$\begin{matrix} 0 \\ 0 \end{matrix}$	$\begin{matrix} \frac{4}{3} \\ -\frac{2}{3} \end{matrix}$	$\begin{matrix} 3 \\ 3 \end{matrix}$
Leptons	$\begin{pmatrix} \nu_e \\ e \end{pmatrix}_L$	$\begin{pmatrix} \nu_\mu \\ \mu \end{pmatrix}_L$	$\begin{pmatrix} \nu_\tau \\ \tau \end{pmatrix}_L$	$\begin{matrix} 0 \\ -1 \end{matrix}$	$\begin{matrix} \frac{1}{2} \\ \frac{1}{2} \end{matrix}$	$\begin{matrix} \frac{1}{2} \\ -\frac{1}{2} \end{matrix}$	$\begin{matrix} -1 \\ -1 \end{matrix}$	$\begin{matrix} 1 \\ 1 \end{matrix}$
	e_R	μ_R	τ_R	-1	0	0	-2	1

Table 1.1: The Elementary Fermions of the Standard Model. Q is the charge, I is the isospin, I_3 is the third component of isospin, and Y is the hypercharge.

1.2 The Standard Model

The Standard Model (SM) [1, 2] of particle physics incorporates three of the 4 forces of nature, the strong force, the electro-magnetic force and the weak force. Gravity has yet to be included. It also describes the fundamental particles. Since the theory was developed in the 1970's, it has been extensively tested, and many of its predictions (such as the $W^{\pm}$ and Z^0 bosons) have come true. Despite this, it is thought that the Standard Model is only an effective theory, one which is valid at certain energies but will fail at others. Therefore, extensions to the Standard Model should be considered as they might complete the picture.

1.2.1 Elements of the SM

The Standard Model is a quantum field theory and describes particles as fields. The particles that make up matter can be thought of as fermion fields which have $\frac{1}{2}$ integer spin and are shown in table 1.1.

The fermions are split into 3 generations with increasing mass (except for the neutrinos) across the generations. Only the first generation is stable

		Gauge and Higgs Bosons		Q	I	I_3	Y	$SU(3)_C$
	γ	*QED*		0	0	0	0	1
	Z^0	*EW*		0	1	0	0	1
Spin 1	W^+	*EW*		1	1	1	0	1
	W^-	*EW*		−1	1	−1	0	1
	$g_\alpha(\alpha = 1.....8)$	*QCD*		0	0	0	0	8
Spin 0	h^0	*Higgs*		0	0	0	0	1

Table 1.2: The vector bosons of the SM

as the heavier particles decay into lighter ones. The particles are further divided as those which interact via the strong, electromagnetic or weak forces are known as the quarks, whilst those that interact via the electromagnetic and/or weak are known as leptons.

There are 6 known leptons, 3 charged (electron, muon and tau) and 3 neutral (neutrinos). Also each charged lepton has an anti-particle with opposite charge, and each neutral lepton has an anti-particle with opposite chirality.

There are 6 known quarks (up, down, charm, strange, top and bottom). Quarks have fractional electric charge and a colour 'charge' (red, blue, green) associated with their interaction via the strong force. There are also 6 anti-quarks which have anti properties such as anti colour, i.e anti blue. Isolated quarks are not observed, but are bound together to form colourless hadrons (either mesons ($q\bar{q}$ state) or baryons (qqq state)).

Only the left handed projections of the fermion fields of each generation can have a weak coupling, so each generation is further grouped into a left handed doublet and a right handed singlet.

Forces are thought to arise as the exchange of integer spin vector bosons. The proposed vector bosons are shown in table 1.2. The massless photon (γ) mediates the electro-magnetic force, whilst the Z^0, W^+ and W^-mediate the

weak force. An octet of massless gluons (g) are responsible for mediating the strong force. The Higgs boson is responsible for giving mass to some of the fundamental particles and will be discussed further in section 1.2.3.

1.2.2 The Gauge theories of the SM

The SM is a relativistic quantum field theory [3] which contains Quantum-Electrodynamics (QED), the Weak force and Quantum Chromodynamics (QCD). These theories may be expressed as local invariance under the transformations of the $SU(3)_C \otimes SU(2)_L \otimes U(1)_Y$ symmetry group. It is the requirement of local invariance that leads to the introduction of new fields which are associated with the exchange of the gauge bosons.

The electro-magnetic force was the first to be described by a gauge theory, and is described by QED which requires local invariance of $U(1)_Q$ transformations. If we start with a global symmetry transformation S and the Quantum-Electrodynamics Lagrangian L_{QED}.

$$\mathrm{S}L_{QED}(\varphi) \rightarrow L_{QED}(\varphi')$$

where S is the symmetry transformation of the U(1) group corresponding to an absolute shift in phase of the field $\varphi' \rightarrow e^{i\theta}\varphi$. The Lagrangian remains invariant. Changing to a local symmetry by introducing space time dependence such that $\mathrm{S} = S(x)$, $x = (\mathbf{x}, t)$ breaks the invariance. To restore the invariance, a further field A_μ needs to be introduced.

$$\mathrm{S}(x)L_{QED}(\varphi, A_\mu) \rightarrow L_{QED}(\varphi', A'_\mu)$$

The changes in the new field A_μ cancel any changes in the L_{QED} and lead to local gauge invariance. The quanta associated with the field A_μ turn out to be massless and are identified to be photons. There are additional interaction terms between φ and A_μ which corresponds to photons coupling with fermions with electromagnetic charge Q. Similarly it is the requirement of local invariance in SU(2) and SU(3) groups which leads to the introduction of the other boson fields.

The weak force requires local invariance under transformations of the $SU(2)_L$ group. The conserved quantity is the third component of weak isospin, I_3. As $SU(2)_L$ is non abelian, the bosons are able to couple to one another.

The strong force is described by QCD, and follows from the invariance of fermion fields under $SU(3)_C$. The conserved quantity is colour and due to the non-abelian nature of the force, the 8 gluons may interact with each other as they carry colour charge.

The strength of the electro-magnetic and weak forces vary with energy and have been shown to become similar at $\tilde{}100GeV$. The two forces are unified in the Standard Model (first postulated by Glashow, Salam and Weinberg [9, 11, 10]) as the Higgs mechanism (see section 1.2.3) causes the mixing of the original weak and electromagnetic fields. Invariance under the transformation of $SU(2)_L \times U(1)_Y$ is required. The conserved quantity of $SU(2)_L$ is again the third component of weak isospin I_3 and invariance under this transformation results in three massless gauge bosons $W_\mu^{1,2,3}$. The conserved quantity of $U(1)_Y$ is hypercharge Y, where $Q = Y + I_3$. Invariance under $U(1)_Y$ results in another massless gauge boson B_μ. Mixing between these

four massless gauge bosons leads to the physical photon field A_μ by

$$A_\mu = sin\theta_w W_\mu^3 + cos\theta_w B_\mu$$

also the physical Z boson field Z_μ by

$$Z_\mu = cos\theta_w W_\mu^3 - sin\theta_w B_\mu$$

and the physical charged $W^\pm$ boson field by

$$W^\pm = \frac{W_\mu^1 \mp iW_\mu^2}{\sqrt{2}}$$

here θ_w is the Weinberg weak mixing angle.

1.2.3 Spontaneous Symmetry Breaking

Spontaneous Symmetry Breaking occurs when a system that is symmetric according to some symmetry group goes into a vacuum state that is non symmetric. It is the mechanism that is able to give mass to the $W^\pm$, and Z^0 bosons without breaking the local gauge invariance of the Standard Model Lagrangian.

The mechanism involves the introduction of a doublet of complex scalar fields $\phi = \begin{pmatrix} \phi_1 \\ \phi_2 \end{pmatrix}$, which causes the potential V to take on the form

$$V(\phi) = \mu^2\phi^2 + \lambda\phi^4$$

λ is a real positive constant and the sign of μ^2 determines the form of

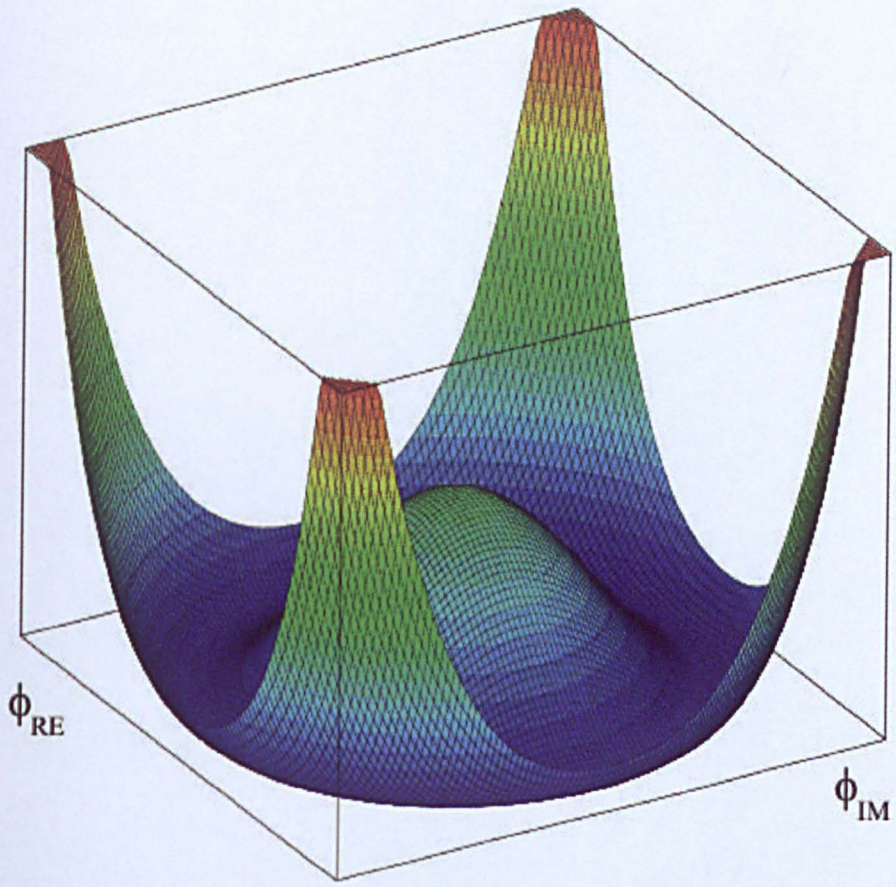

Figure 1.1: Higgs potential with the potential displayed with real and imaginary parts. It is worth noting that the minimum is not where the fields vanish Taken from [22]

the potential. Interestingly if μ^2 is negative then the potential is of the form of a Mexican hat function (as shown in figure 1.1), and the minimum or Vacuum Expectation Value (VEV) is not at the origin where the fields vanish, but can be located at any point on a circle of radius $\sqrt{\frac{\mu^2}{2\lambda}}$. The electroweak Lagrangian (L_{EW}) is invariant under rotation in the ϕ_1, ϕ_2 plane. The system also has an unstable vacuum state corresponding to $\phi = 0$. It is once the system falls into a stable vacuum state, or point on the circle that the symmetry is lost. Now, fluctuations around the particular minimum will lead to terms which imply one massive scalar known as the Higgs boson, and three extra degrees of freedom. The three extra degrees of freedom give mass to the $W^{\pm}$, and Z^0 bosons whilst the photon stays massless.

A scalar field has been introduced as a mechanism for spontaneous symmetry breaking, and the result is giving mass to the weak force carriers and the existence of a new physical boson, the Higgs boson. This mechanism does not predict the mass of any of the bosons, only the ratio of the W to the Z mass as $cos\theta_w$. This has been experimentally verified, however the Higgs has not been discovered by any experiment so far. Unitarity constraints of W^+W^- scattering place the upper limit on the mass of the Higgs at $\sim 1\ TeV$[13]. Precision fits from electroweak data give the upper limit of 219 GeV to 95% CL. [14] LEP placed the lower limit of the Higgs mass at 114.4 GeV 95% CL [15]which was added to at the Tevatron by excluding a range around 170 GeV 95% CL. This suggests we have a good chance of finding the Higgs at the LHC.

1.3 SUSY

SUper-SYmmetry (SUSY) [17, 18] is a hypothetical symmetry which takes the symmetries observed in nature one step further. SUSY introduces a new operator **Q** which turns a fermionic state into a bosonic one and vice versa via

$$\mathbf{Q}|Boson>=|Fermion> \qquad \mathbf{Q}|Fermion>=|Boson>$$

Therefore if SUSY is realised in nature, every particle in the SM has a super-partner with the same internal quantum numbers but differing by a half integer spin.

SUSY is an attractive theory because it solves problems with the Standard Model such as the Technical Hierachy problem, unification of the gauge couplings at the GUT scale, and the existence of dark matter.

The Technical Hierarchy problem

We have already seen that the Higgs mass must be less than $\sim 1\ TeV$ due to unitarity constraints of W^+W^- scattering. However, the SM predicts that the Higgs mass will be subject to large radiative corrections [12]. The existence of a fermion with mass m_f which has a coupling constant to the Higgs of λ_f will give a correction to the square of the Higgs mass of

$$\delta M_H^2 = \frac{|\lambda_f|^2}{16\pi^2}\left[-2\Lambda^2 + 6m_f^2 ln\left(\frac{\Lambda}{m_f}\right).....\right]$$

here Λ is the energy cut off scale where the new the theory breaks down.

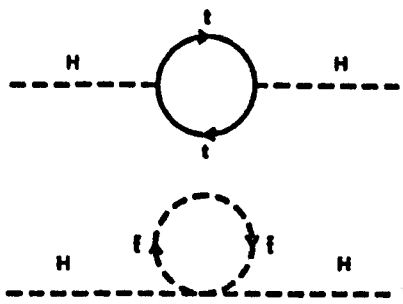

Figure 1.2: Loop corrections to the SM Higgs mass

If Λ is assumed to be the Planck scale then it has a value of $\sim 10^{19} GeV$ which gives a huge Higgs mass. A large amount of fine tuning is then needed to get a mass of $\sim 100 GeV$.

This problem can be overcome if each fermion has a bosonic partner. Such boson loops would contribute to the mass calculation with opposite sign, thereby neatly cancelling the contribution of the fermion loops as can be seen in figure 1.2.

Grand Unified Theories

Another property of SUSY is the possible unification of the gauge field coupling constants at the grand unified (or GUT) scale. The evolution of α_1, α_2 and α_3 from the electroweak scale is shown in figure 1.3 as a function of sliding scale Q in GeV. It can be seen that the couplings do not converge if no new particles are assumed to exist above the electroweak scale. If modifications to gauge couplings are taken into account by introducing SUSY at around the TeV scale it is found that the values will unify at a point within experimental bounds.

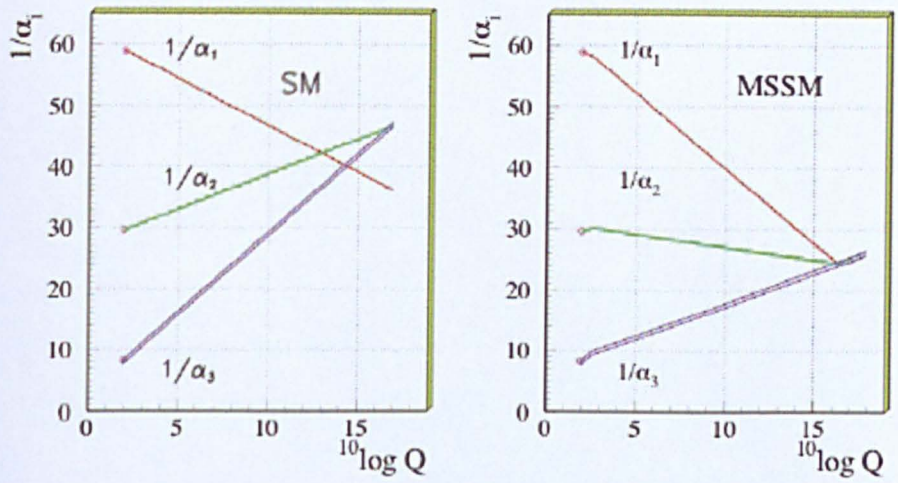

Figure 1.3: Renormalisation group running of the inverse gauge couplings α_i^{-1}, in the SM (left), and MSSM (right). α_1 is the electro-magnetic coupling, α_2 is the weak coupling constant and α_3 is the strong coupling constant. These are plotted against the logarithm (base 10) of Q, which is the energy scale taken from [7]

1.3.1 Elements of the MSSM

The Minimal Supersymmetric Standard Model is a SUSY model with the minimum number of additional particles to the SM. The particles are shown in table 1.3. Each known particle has a super partner. For fermions the partners are scalar (spin 0) particles known as sfermions, whilst for bosons the partners are spin $\frac{1}{2}$ particles known as gauginos. The naming convention is such that the super partners of the fermions have the prefix s-, and the super partners of the bosons have the post-fix -ino. When representing a particle with a symbol, convention dictates that a tilde ˜ is used. As the fermions in the SM have chirality, each different state has its own super partner (e.g $u \rightarrow \tilde{u_L}, \tilde{u_R}$), (As right handed neutrinos are thought not to exist in the SM the sub-script may be dropped from the sneutrino ($\tilde{\nu}$) if

Standard Model particles			Supersymmetric partners				
			Weak Eigenstates			*Mass Eigenstates*	
Name	Symbol	Spin	Name	Symbol	Spin	Name	Symbol
Fermions			**Sfermions**				
Leptons	l	$\frac{1}{2}$	Sleptons	$\tilde{l}_L, \tilde{l}_R$	0		$\tilde{\tau}_1, \tilde{\tau}_2$
Neutrinos	ν_l	$\frac{1}{2}$	Sneutrinos	$\tilde{\nu}_l$	0		
Quarks	q	$\frac{1}{2}$	Squarks	$\tilde{q}_L, \tilde{q}_R$	0		$\tilde{t}_1, \tilde{t}_2, \tilde{b}_1, \tilde{b}_2$
Neutral Gauge Bosons			**Neutral Gauginos**				
Photon	γ	1	Photino	$\tilde{\gamma}$	$\frac{1}{2}$	Neutralinos	$\tilde{\chi}_i^0$ $(i = 1, 4)$
Neutral Weak	Z^0	1	Zino	$\tilde{Z}^0$	$\frac{1}{2}$		
Neutral Higgs	h,H,A	0	Neutral Higgsinos	$\tilde{H}^0_{1,2}$	$\frac{1}{2}$		
Gluons	$g_{1,8}$	1	Gluinos	$\tilde{g}_{1,8}$	$\frac{1}{2}$		
Gravition	G	2	Gravitino	$\tilde{G}$	$\frac{3}{2}$		
Charged Gauge Bosons			**Charged Gauginos**				
Charged Weak	$W^\pm$	1	Wino	$\tilde{W}^\pm$	$\frac{1}{2}$	Charginos	$\tilde{\chi}_i^\pm$ $(i = 1, 2)$
Charged Higgs	$H^\pm$	0	Charged Higgsinos	$\tilde{H}^\pm$	$\frac{1}{2}$		

Table 1.3: The MSSM particles. H is a SM particle, whilst $H^\pm$, A, and h are SUSY.

neutrinos have no mass).

An extension needs to be made to the Higgs field which was introduced in section 1.2.3 to allow symmetry breaking. In the MSSM there are two Higgs doublets (H_u, H_d) which have one charged and one neutral massive component each. These have corresponding super partners, the higgsinos.

The charginos ($\tilde{\chi}_i^{\pm}$) and neutralinos (χ_i^0) are formed by mixing which occurs between the gaugino super partners of the weak gauge bosons as shown in table 1.3.

1.3.2 Super-symmetry breaking

SUSY and more specifically the MSSM postulates that each particle has a super-symmetric partner. Clearly this cannot be a perfect symmetry. Whilst the charge, weak isospin and degrees of freedom can be the same in each of these particles, the new super-partners do not have the same mass. If they were to have the same mass evidence supporting the existence of such particles would have already been observed. For example smuons and selectrons with masses $< 100\ GeV$ have been excluded. Super-symmetry must therefore be a broken symmetry [21].

To maintain SUSY as a viable solution to the hierarchy problem, it must be broken in such a way that the divergences discussed earlier still cancel. This can be done by the addition of a soft breaking term. These include the explicitly added mass terms which must not be too large compared to the masses of the Standard Model particles to maintain a solution to the hierarchy problem.

The Lagrangian for the MSSM is then

$$L_{MSSM} = L_{SUSY} + L_{soft}$$

here, L_{SUSY} contains the SUSY conserving terms, whilst L_{soft} is SUSY violating.

Defining the Lagrangian in this way allows for something that is analogous to electro-weak symmetry breaking as discussed in section 1.2.3. The Lagrangian is invariant whilst the Vacuum Expectation Value (VEV) is not. It is worth noting that SUSY breaking occurs in a high energy region (hidden sector) away from the electro-weak scale (visible sector). There are different methods for the exact mechanism that SUSY breaking is communicated to the visible sector, but this can remain open without a loss to the predictive power.

Popular models include minimal Super Gravity (mSUGRA) [19] where SUSY is broken by gravitational interactions, and Gauge Mediated Super symmetry breaking [21] where SUSY is broken by gauge interactions. Another popular model is Anomaly Mediated Super symmetry breaking (AMSB) [21].

Super Gravity

This thesis presents a study of gravity mediated Super-symmetry breaking. Particles in both the hidden and the visible sector couple to gravitational interactions so it is consistent that gravity could act as the messenger of Super-symmetry breaking. In particular this thesis presents a constrained

version of gravity mediated Super-symmetry (mSUGRA) [19]. In this case the number of free parameters has been reduced by assuming the soft breaking parameters are universal at the GUT scale. An example of this is that all the mass parameters are reduced to a common gaugino mass $m_{\frac{1}{2}}$ and a scalar mass m_0. The masses of all the MSSM particles are then evolved from unification down to the electroweak scale by Renormalisation Group Equations as shown in figure 1.4. There are now only 5 free parameters:

- m_0 - Common scalar mass.
- $m_{\frac{1}{2}}$ - Common gaugino mass.
- $tan\beta = \frac{\nu_1}{\nu_2}$ where ν_1 and ν_2 are the VEV for the Higgs coupling to the up and down type particles
- μ - Higgs-higgsino mass parameter.
- A_0 - Common third generation trilinear Higgs interaction term.

1.3.3 R Parity

Lepton and Baryon number violation are not expressly forbidden by the MSSM. Experimental evidence shows that the lower limit on the proton lifetime is 1.6×10^{33} years hinting that that baryon and lepton numbers must be conserved. To add this conservation law to the MSSM, a new symmetry known as R-parity [20] is introduced.

$$R = -1^{3(B-L)+2S}$$

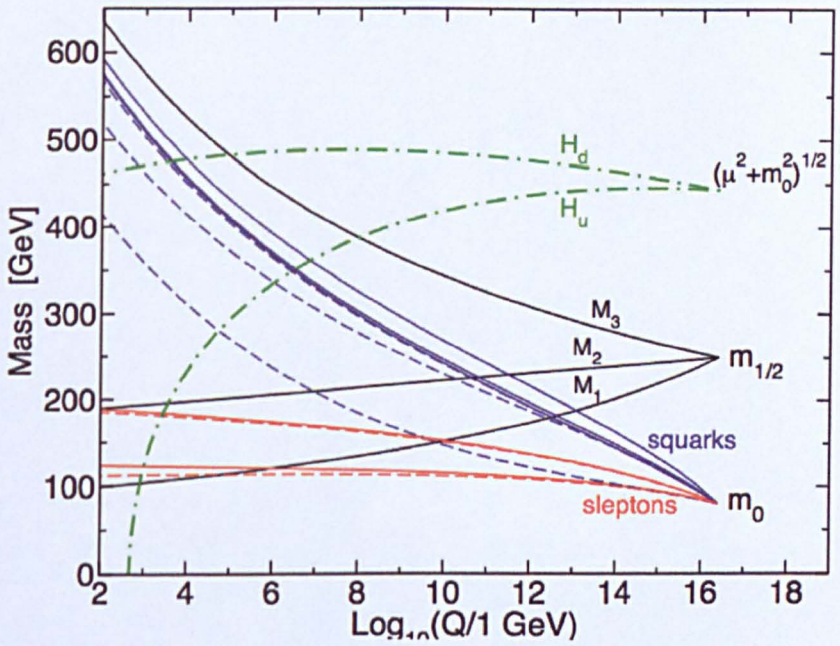

Figure 1.4: Evolution of MSSM particles (scalar and gaugino mass parameters) from the GUT scale to the EW scale. This is with a typical minimal supergravity-inspired boundary conditions imposed at $Q_0 = 2.5 \times 10^{16} GeV$. The parameter $\mu^2 + m_{H_u}^2$ runs negative, provoking electroweak symmetry breaking. μ is the Higgs-higgsino mass parameter, $m_{\frac{1}{2}}$ is the common gaugino mass, and M_1, M_2, and M_3 are examples of gauginos. Q is the energy scale in GeV. Taken from [17]

where B is the baryon number, L is the lepton number and S is the spin. Note that SM particles have even R-parity, whilst SUSY particles have odd R-parity.

R-Parity can be either conserved or not depending on the model being studied. In the mSUGRA SUSY variant R-Parity is conserved. This has several consequences. As SM particles have even R-Parity and their super-partners have odd R-Parity, sparticles may only be produced in pairs. Secondly, the Lightest Super-symmetric Particle (LSP) is stable, and finally all sparticles other than the LSP will eventually decay into an odd number of LSP's. For most of SUSY parameter space the LSP is χ_1^0. Being stable and weakly interacting the χ_1^0's left from the big bang would persist throughout the universe and not decay. This provides a possible explanation for observed dark matter.

1.4 Summary

The Standard Model has been introduced as an effective theory which is only appropriate for certain energy scales. It is thought that the model breaks down at higher energies. SUSY is presented as an attractive extension to the SM, by adding an extra symmetry. An onslaught of super-partner particles are summoned to satisfy this symmetry.

SUSY solves some of the problems with the SM, such as the technical hierarchy problem and the existence of dark matter. The next generation of particle detectors at the LHC are set to reveal if this is the way that nature works.

Chapter 2

Atlas and the LHC

In 1954, CERN, the European Organisation for Nuclear Research first opened. Today, CERN is one of the largest science laboratories in the world and hosts about 10,000 physicists from over 80 countries. CERN has been home to many particle accelerators, but none as high energy as the new Large Hadron Collider or LHC. Here particles will be accelerated to unprecedented energies and collided at various interaction points which house huge detectors that will study the results of the collisions.

2.1 The LHC

The LHC, shown schematically in figure 2.1 is the largest operational particle accelerator and collider in the world. The 10th of September 2008 was a special day for CERN and indeed the LHC. For the first time, two counter rotating proton beams were circulated separately around the 27 km long LEP tunnel, which is 100m deep under the Swiss-French border. The LHC is

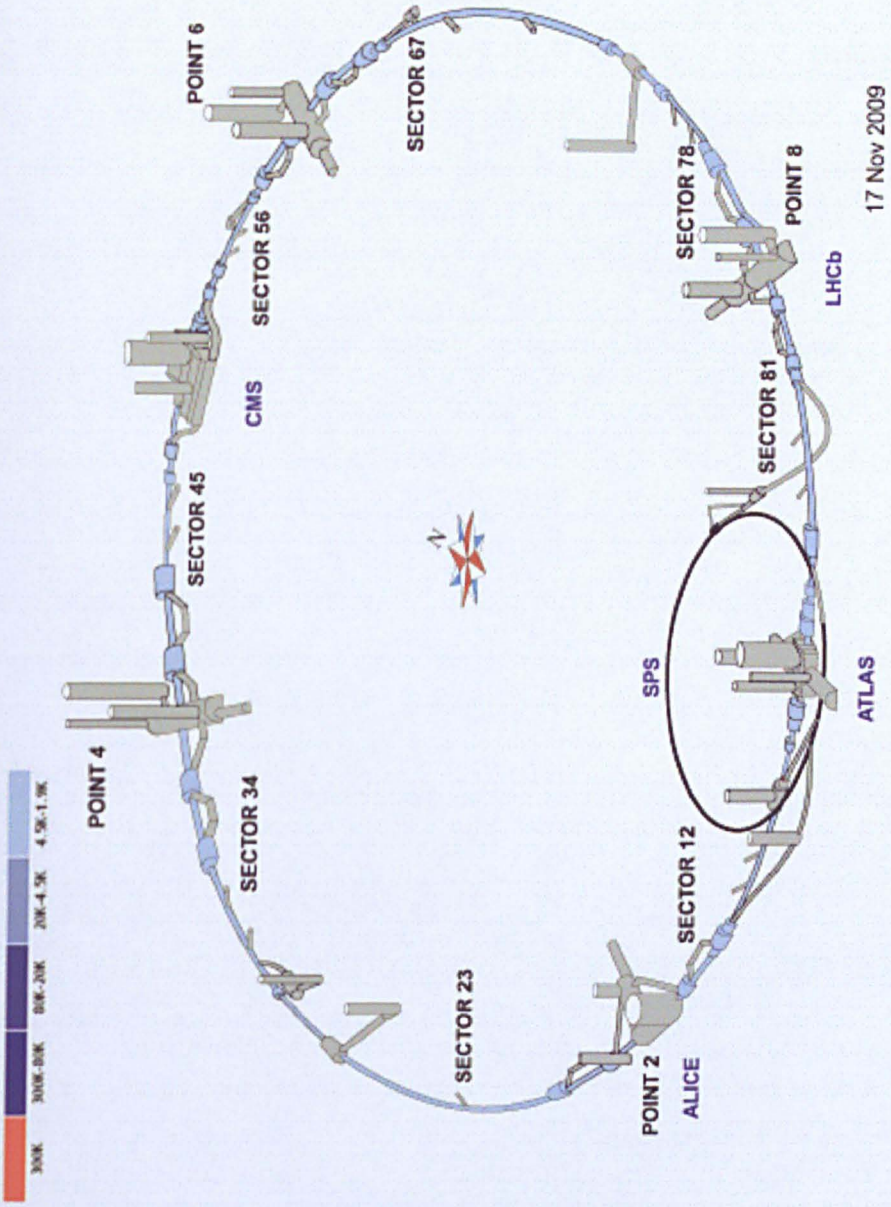

Figure 2.1: The LHC and the interaction points where the experiments are situated. Areas in red show new civil engineering from the LEP experiment. Taken from [23]

designed to accelerate protons up to 7 TeV (which then collide with a centre of mass energy of 14 TeV). This is 7 times greater than the Tevatron which holds the previous record.

Before the protons are injected into the LHC, they are first accelerated by various sub-systems. First a small linac and booster is used and from there they are injected into the proton synchrotron (PS). The PS accelerates them up to 26 GeV and it is then the Super Proton Synchrotron (SPS) that accelerates them to 450GeV. The protons are then injected into the LHC where they reach 7 TeV. The beams are not a continuous spread of protons, rather they are divided up into 2808 bunches, so that interactions occur between the two beams at discrete intervals. At full luminosity, there are 4×10^7 bunch crossings per second. A tiny fraction of these result in collisions producing high mass objects in which we are interested but in each bunch crossing there are also ~ 23 other collisions, inelastic pp interactions which are known as pile up.

There are 4 detectors situated around the ring, ATLAS (A Toroidal LHC ApparatuS), CMS (Compact Muon Solenoid), LHCb (LHC beauty experiment) and ALICE (A Large Ion Collider Experiment). The two largest of these detectors (ATLAS and CMS) are general purpose detectors and are optimised for the detection of new physics. LHCb is designed to study b-physics, and finally ALICE will investigate strong interactions at extreme densities as the LHC can also accelerate beams of heavy ions, e.g. Pb.

Collisions are planned for the LHC by the end of November 2009. Initial plans were to have centre of mass of 10 TeV collisions, with a luminosity of $10^{31} cm^{-2} s^{-1}$. Initially, the LHC was going to run throughout the winter

Energy at collision	7.0 TeV
Energy at injection	0.45 TeV
Machine circumference	26658.833 m
Dipole field at 7 TeV	8.33 T
Time between bunches (at $L = 10^{34} cm^{-2} s^{-1}$)	25 ns
Number of particles per bunch	1.15×10^{11}
Number of bunches per beam	2808
RMS bunch length	7.55 cm
Circulating beam current	0.582 A
Dipole magnet temperature	1.9 K
Number of dipole magnets	1232
Number of quadrupole magnets	approx 600

Table 2.1: Parameters for the LHC running in proton-proton collision mode at design luminosity taken from [24]

and $\sim 200 pb^{-1}$ would have been expected for within a year. In Autumn 2010, following a short shutdown, the centre of mass energy was going be increased to 14 TeV, and the luminosity to $10^{33} cm^{-2} s^{-1}$. After a few years of operation the design luminosity of $10^{34} cm^{-2} s^{-1}$ would finally be reached. The new plans are for the LHC to start with a centre of mass energy of 7 TeV and slowly increase in energy and luminosity.

Some parameters of the LHC are shown in table 2.1 which illuminates the sheer technical challenge undertaken in building such an experiment.

2.2 The ATLAS experiment

ATLAS measures 46 m in length and 25 m in diameter, and weighs 7,000 tonnes. Roughly 2000 scientists and engineers work on the project from 165 institutions in 35 countries. Figure 2.2 shows a diagram of the ATLAS detector. A right handed Cartesian co-ordinate system may be applied to the

ATLAS detector as follows. The z-axis is defined as being along the beam with the positive x-axis pointing towards the centre of the ring, and the positive y-axis pointing in the upward direction. The shape of the detector is almost exactly cylindrical and as such lends itself to the use of cylindrical coordinates i.e. (r,ϕ,z), with R being the transverse radius from the beam-line, ϕ the azimuthal angle from the x-axis, and the origin of the z-axis is at the interaction point. It is also useful to define the polar angle θ which is measured from the z-axis.

ATLAS has been designed to search for new physics, and as such it can detect and measure a wide range of particles. It can directly detect charged and most neutral particles that are produced from the decay of unstable SM particles and the particles possibly produced according to new theories. ATLAS can also infer the presence of neutral particles which only interact via the weak force, such as the neutrino. As direct observation of these particles is almost impossible, the hermiticity of the detector may be used to make a measurement of missing transverse (ie. perpendicular to the beam) energy or E_T^{miss} thus inferring the presence of these particles.

In a collision, it is the individual partons that interact. The momentum carried by individual parton varies, and may be quantified by parton distribution functions [25]. These state the probabilty density for finding a parton with momentum fraction x at momentum transfer Q^2. Thus, since the colliding partons typically carry different fraction of the proton momentum, the centre of momentum of the collision will usually be moving rapidly along the beam axis. However, because the partons start with almost zero momentum transverse to the beam, the total transverse momentum should be close to

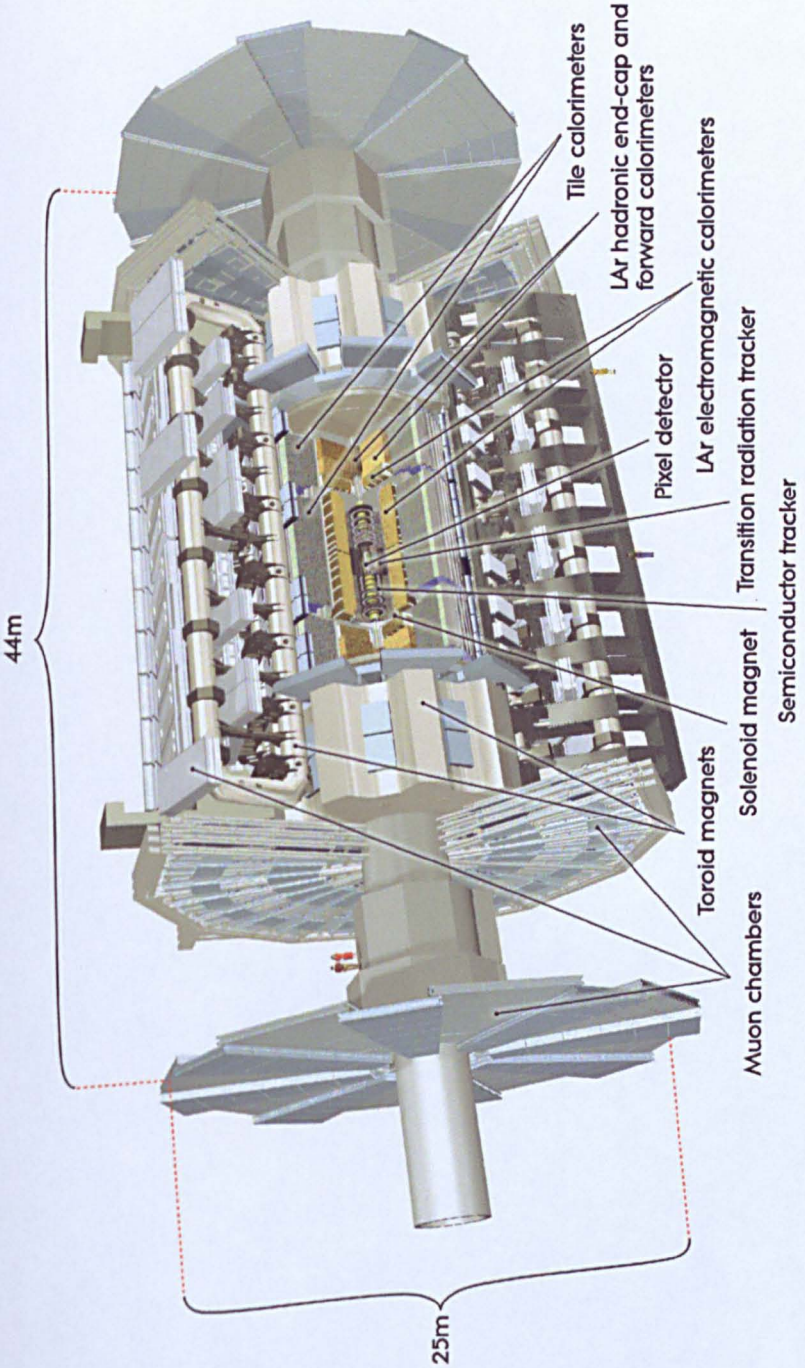

Figure 2.2: Labelled diagram of the ATLAS detector showing the major sub-detectors

zero.

It is useful to define the following quantities.

- The rapidity of a particle is given by $y = \frac{1}{2} ln\left[(E + p_z)/(E - p_z)\right]$. This is useful because differences in the rapidity's of a particle are invariant under longitudinal Lorentz boosts (such as boosts connecting the lab and the centre of mass frames).

- The pseudo-rapidity, given by $\eta = -ln[tan(\frac{\theta}{2})]$ approximates the true rapidity in the relativistic limit where particle masses can be neglected.

The momenta of particles in the ATLAS detector are frequently expressed using the parameters (p_T,η,ϕ) with $p_T = \sqrt{p_x^2 + p_y^2}$. The relationship $\Delta R = \sqrt{\Delta\eta^2 + \Delta\phi^2}$ refers to the distance that the particles are separated by in the $\eta - \phi$ plane.

Unlike LHCb and ALICE, ATLAS is a general purpose physics detector built with the intention of accommodating as wide a physics program as possible. This program will include precision tests of the Standard Model, and also searches for new physics. An in depth description of the ATLAS detector and all the various sub-systems including the quoted resolutions may be found in [26].

2.2.1 The Magnet System

Magnets are used in particle detectors to bend charged particles so that their momenta may be measured. The radius of curvature, r (metres) is related to the particle momentum, p (measured in GeV/c) and the magnetic field B (in Tesla) by:

$$p = 0.3Br$$

By measuring the curvature of the particles path, an estimate of their momentum is obtained.

The magnet system at ATLAS is divided into two separate systems, the inner solenoid and the outer toroidal magnet. The magnet coils are made of Al stabilised Nb-Ti superconductor operating at 4 K. The magnets will be cooled to this temperature using liquid helium.

The inner solenoid surrounds the inner detector and is designed to be as thin as possible to minimise the radiation lengths that the particles must cross before they reach the calorimeters. This means that whilst the magnet is 5.3 m long with a radius of 1.15m the thickness is only 45mm. Producing a field strength of 2 T enables the inner detector magnet to accurately measure a particle's momentum up to 100 GeV and down to 400 MeV. Below this the particle will not be measured due to looping repeatedly in the field. Above 100GeV the deviation from a straight line is too small for the tracking detectors to measure accurately.

The outer toroidal magnet is the most visually stunning aspect of the detector. This magnet system comprises of 8 very large air core superconducting barrel loops and 2 end caps and are situated outside the calorimeters and are populated with the muon detectors. Whilst not uniform, the average field in the muon spectrometer of 0.6 T allows muons with high momenta to be measured.

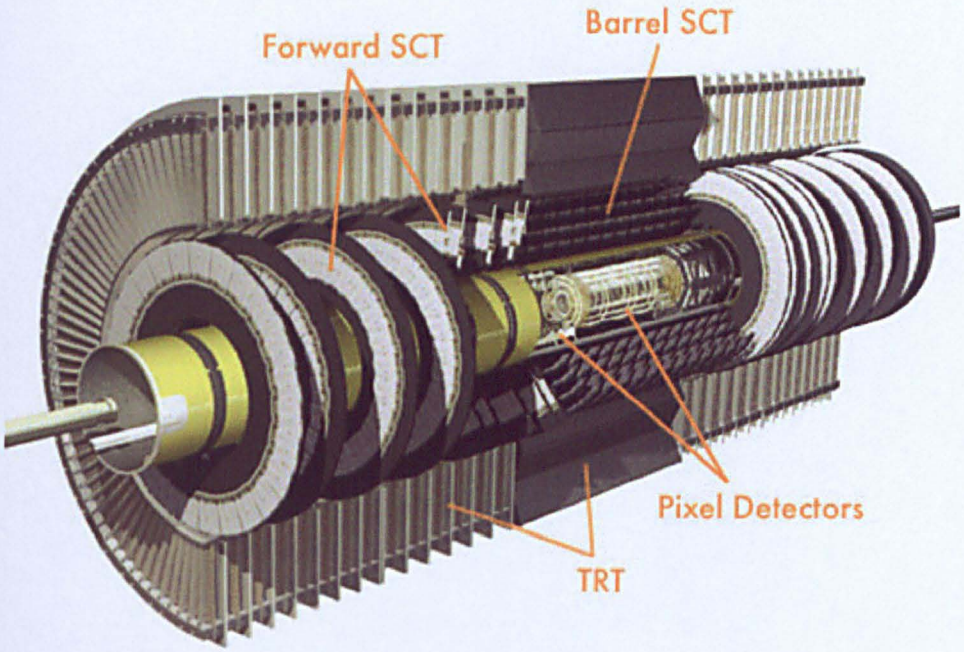

Figure 2.3: A cut away of the inner detector showing the Pixel Detector, the SCT, and the TRT

2.2.2 The Inner Detector

The Inner detector shown in figure 2.3 is designed to accurately measure particle's momenta, charge, and to determine whether they were produced at a primary or secondary vertex (detection of the vertex is important for B-tagging). The inner detector is divided into 3 parts: the pixel detector; the semi-conductor tracker (SCT); and the transition radiation tracker (TRT), and covers $|\eta| < 2.5$.

The Pixel detector

The Pixel Detector is the closest part of the detector to the beam line. It consists of 3 layers (one "B-layer," and two barrel layers) situated at 50.5

mm, 88.5 mm and 122.5 mm from the beam, with 3 disks on each end-cap. The Pixels are designed to be smaller in the $R\ \phi$ plane to give a better measurement of the sagitta (curve) of the particle tracks to give a better measurement of the momentum.

The detector has a total of 1744 modules, each of which measures 2cm by 6cm. Each module is made of a silicon pixel array bump-bonded to 16 front-end integrated read out circuits and is 250 μm thick. There are roughly 47,000 pixels per module, and each pixel is of size 50×400 μm. This tiny pixel size gives high granularity and good vertex resolution. It is the high cost per covered area that prohibits the use of this detector at higher radius.

As the pixel detector is closest to the beam it receives the highest doses of radiation. Thus, it must be designed to be as radiation hard as possible. The 140 million pixel channels allow the reconstruction of events in this high occupancy environment. Due to radiation damage the B-layer is designed to be replaced every few years.

The SCT

The SCT (Semi-Conductor Tracker) provides measurements between the pixel detector and the TRT. It uses the same basic principle for detection as the Pixel Detector, but uses silicon strips rather than pixels in order to cover a larger area. It needs fewer read out channels (62 million) than the Pixel Detector due to the decrease in track multiplicity at higher radius.

The SCT barrel is made up of 63.6×64 mm modules containing parallel silicon microstrips with a 80 μm pitch. The strips are aligned parallel to the beam axis. Two silicon wafers are glued back to back with an offset in the

stereo angle of 40 *mrads* allowing for precision measurements in $R\ \phi$ and z. The end-cap modules are similar but with the micro-strips arranged radially. A SCT module has a resolution of 16 μm in $R\phi$ and 66 μm in z (barrel) and 77 μm in R (end-caps).

The TRT

The Transition Radiation Tracker (TRT) is the part of the inner detector furthest out from the interaction point. Due to the cost of covering such a large area, and the relatively low track density there, the TRT is designed to use "straw" detectors. These are cylindrical tubes with a diameter of 4mm and a maximum length of 144cm. They are filled with a mixture of Xe, CO_2, and O_2 and have a gold plated tungsten wire running down the central axis along the length of the tube. The insides of the tube are coated with aluminium. The aluminium acts as a cathode whilst the central wire acts an anode. An applied electric field across the anode and cathode acts to amplify electric charge produced by ionisation as charged particles traverse the gas.

The space between the straws is filled with polypropylene. This adds to the amount of transition radiation in the detector (produced when relativistic particles cross a boundary between materials with different dielectric constants). Transition radiation interacts with the gas and it is possible to distinguish between electrons and hadrons in this detector because the transition radiation is produced by electrons when their momentum is close to 1 GeV, whilst pions only start to radiate when their momentum is nearly 100GeV.

2.2.3 Calorimeters

The ATLAS calorimeters (shown in figure 2.4) have the job of stopping and precisely measuring the energy of charged and most neutral particles. ATLAS has an electromagnetic (ECAL) and a hadronic calorimeter (HCAL), each designed for different particles. The nuclear inteteraction length is defined as the mean free path to reduce the energy of relativistic particles by $\frac{1}{e}$, and the electromagnetic radiation length X_0 is defined as the mean distance over which a high energy electron loses all but $\frac{1}{e}$ of its energy by bremsstrahlung. As the average λ is roughly ten times X_0, the ECAL is inside the HCAL.

Both calorimeters are sampling calorimeters. That is the material used to initiate the shower is distinct from that which measures the showers energy. The two materials, both passive absorber and active readout, are set in layers, and thus the energy lost by particles sampled as they traverse the calorimeter. The calorimeters are also non-compensating, that is they react differently to electromagnetic and hadronic showers and this must be accounted for in the offline software.

EM calorimeter

The ECAL is designed to contain and measure electrons and photons. It consists of a barrel and two end caps. The barrel has a radius from 2.8m to 4m and is made of two sections each of which is 3.2 m long. It covers a $|\eta| < 1.475$. The end caps both have an inner and and outer disk. The outer disk covers $1.375 < |\eta| < 2.5$ and the inner disk covers $2.5 < |\eta| < 3.2$. There are cracks at $|\eta| = 0$ and $1.37 < |\eta| < 1.52$. To ensure that the electrons are

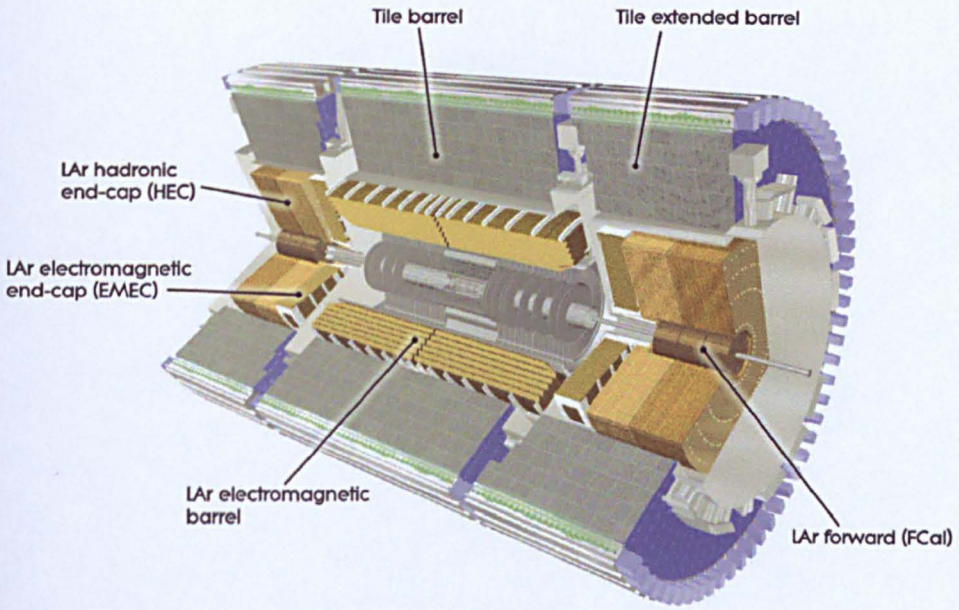

Figure 2.4: A schematic of the ATLAS Calorimeters

fully contained and measured the ECAL is over 22 radiation lengths long in the barrel and more than 24 in the end caps.

Made of lead (to initiate the shower), and liquid argon (to measure the energy), the ECAL is intrinsically radiation hard. The accordion geometry avoids gaps in ϕ coverage which is a necessity for E_T^{miss}measurements. There is a presampler layer of liquid argon with strip readout which ensures that any showers which have started before reaching the ECAL can be properly corrected. The energy resolution in the ECAL is $\sigma_E/E = 10\%/\sqrt{E} \oplus 0.7\%$.

Hadronic calorimeter

The HCAL is designed to initiate and measure hadronic showers. It is an average of ten nuclear interaction lengths wide to contain the showers and

prevent leakage into the muon system. The HCAL is made up of a central barrel which covers $|\eta| < 0.8$ and two extended barrels which extend the coverage to $|\eta| < 1.7$. The barrel calorimeters are made of steel and have plastic scintillator sheets inserted throughout their volume. The end caps have 2 disks each and cover a range $1.5 < |\eta| < 3.2$. Due to the higher radiation received by this part of the HCAL, it is composed of copper and liquid argon which are more radiation hard. The forward calorimeter receives an even higher dose of radiation as it covers $3.1 < |\eta| < 4.9$. It has sheets of tungsten which are interspersed with sheets of copper and liquid argon.

The energy resolution of HCAL is $\sigma_E/E = 50\%/\sqrt{E} \oplus 3\%$ for the barrels and end-caps and the forward calorimeter has a resolution of $\sigma_E/E = 100\%/\sqrt{E} \oplus 10\%$.

2.2.4 Muon detectors

The ATLAS detector is designed so that only muons and neutral weakly interacting particles reach the muon spectrometer. In fact, a muon must have momentum greater than 3 GeV to reach the muon chambers. The muon spectrometer consists of 3 barrel layers with radii of 5 m, 7.5 m, and 10 m. The barrel covers $|\eta| < 1.0$. The end caps have 4 layers and cover $1.0 < |\eta| < 2.7$.

The aim of the muon chambers is to provide precise tracking and a trigger for muons. Due to the large distance that the chambers are from the interaction point, the system will be optically aligned and corrections can be made to the track positions in the offline code. To achieve its aims, four different

technologies are employed for measuring muons. Two of these constitute the precision measurement chambers. They are Monitored Drift Tubes or MDTs in the low $|\eta|$ barrel and end caps, and Cathode Strip Chambers or CSCs which cover $2 < |\eta| < 2.7$ due to the higher particle flux. The trigger is formed of Resistive Plate Chambers or RPCs in the barrel, and thin Gap Chambers (TGCs) in the end cap.

2.2.5 The Trigger and DAQ systems

Every event at ATLAS contains information about 'hits' and energy depositions in the detector. At 1.3 megabytes each, it is not possible to record every event to disk due to the collossal number of events per second. It is therefore the role of the trigger and DAQ system to reduce this rate, whilst still recording interesting collisions. A trigger menu contains a list of requirements that an event must meet to be written to disk, and consists of criteria such as the existence of a high p_T electron or muon, or a large E_T^{miss}. It is possible to change the trigger selection in case new physics is found or the luminosity of the LHC changes. The relevant trigger menus and rates for the analysis presented in this thesis and for a luminosity of $10^{31} cm^{-2} s^{-1}$ may be found in tables 2.2 - 2.4 [27]. The notation used is EM (electromagnetic), J (Jets), XE (E_T^{miss}). The numbers in the trigger item indiciate the required transvere momentum for the item, and an I in the trigger item indicates that the item must be isolated. The prescale is the number of events of that type that need occur before one is stored to disc. This is again to reduce that amount of data stored. The study of the resolution on the E_T^{miss} in chapter

Trigger Item	EM3	EM7	EM13	EM13I	EM18	EM18I	EM23I	EM100
Prescale	60	1	1	1	1	1	1	1
Rate (Hz)	674	4900	950	480	369	143	53	1.5
Trigger Item	2EM3	2EM7	2EM13	2EM13I	2EM18	2EM18I	2EM23I	3EM7
Prescale	1	1	1	1	1	1	1	1
Rate (Hz)	6500	534	108	8	47	2	0.6	53

Table 2.2: Electro-magnetic trigger items and estimated rates at luminosity of $10^{31} cm^{-2} s^{-1}$

Trigger item	J10	J18	J23	J35	J42	J70	J120	3J10	3J18	4J10	4J18	4J23
Prescale	42000	6000	2000	500	100	15	1	150	1	30	1	1
Rate (Hz)	4	1	1	1	4	4	9	40	140	40	20	7

Table 2.3: Jet trigger items and estimated rates at luminosity of $10^{31} cm^{-2} s{-}1$

4 will use the electron triggers, and as the SUSY study in chapter 5 requires high P_T jets and E_T^{miss}, it will use the jet and E_T^{miss} triggers.

The trigger layout is shown in figure 2.5 and is has 3 levels [27]. They are know as the Level 1 (L1), Level 2 (L2), and Event Filter (EF). These systems work together to reduce the event rate from a bunch crossing rate of 40 MHz to 200 Hz.

L1 is hardware based and uses reduced granularity calorimeter information. It also uses the muon spectrometer trigger system. It does not, however, use the tracking system of the inner detector. The L1 trigger reaches a decision in 2.5 μs, and reduces the rate to $75 - 100$ KHz. L1 passes the decision to the L2 trigger, and also specifies any Regions of Interest (ROIs) which are

Trigger item	XE15	XE20	XE25	XE30	XE40	XE50	XE70	XE80
Prescale	30000	7000	1500	200	20	2	1	1
Rate (Hz)	2.5	3	4	7.5	7.5	14	2	1

Table 2.4: E_T^{miss}trigger items and estimated rates

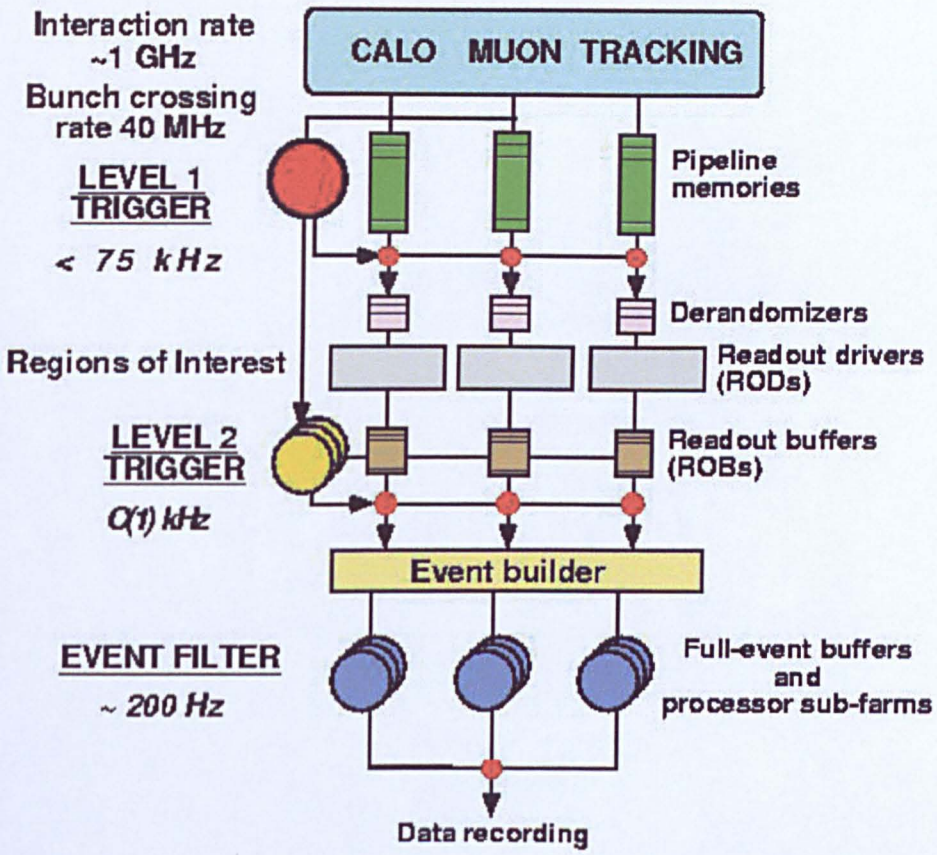

Figure 2.5: Diagram of the ATLAS trigger/DAQ system

sections of the detector in which a particle traversed. If an event passes the L1 trigger, L2 uses high precision information from the detector, including tracking but only in the ROIs. The L2 trigger takes 40ms to make a decision, and reduces the rate to 3.5 KHz. The event is then passed to the EF which uses the full detector information including vertexing and reconstructed E_T^{miss}. It takes as long as 4s to decide if the event is to be written to disk, and reduces the rate to 200Hz.

2.3 Summary

The LHC and ATLAS have been introduced, and how some of the challenges facing the experiment are overcome. With the current schedule of November 2009 for the first collisions it is anticipated that a new era of physics is beginning. ATLAS is a state of the art detector, which provides accurate tracking, good calorimetry, and a precise muon system.

Chapter 3

Analysis Framework

3.1 Introduction

As discussed in chapter 2, massive accelerators and detectors are used in the study of particle physics. The studies undertaken in this thesis do not include real data from the experiment (at the time of writing there have been no collisons), rather they focus on detailed simulations of the interactions that will take place in the detector. Using these simulations it is possible to predict what might happen when real data is present.

There are two main ideas behind a simulation which are listed below.

1. Event Generation: From a parton model of a proton, with momentum shared amonst the partons following a PDF set, Monte Carlo generators are used to simulate the physical processes from the initial state to the final state. The underlying event (everything except the two outgoing hard scattered jets) also needs to be simulated. Also hadronisation (the 'freezing out' of quarks) processes are simulated. The generators used

in this thesis are-

- HERWIG (Hadron Emission Reactions With Interfering Gluons) [28, 29]: was used to generate the SUSY events. As Herwig does not describe the entire event Jimmy [30] was used to simulate the underlying event. The events were NLO and the PDF set used was CTEQ6LI [31]
- PYTHIA [32]: This generator was used to simulate the $Z \rightarrow \nu\nu$ sample. It is a LO generator. The signal was weighted to an integrated luminosity of $1fb^{-1}$ according to cross-section. PYTHIA also describes the underlying event. The PDF set used was CTEQ6LI.
- MC@NLO (Monte Carlo At Next to Leading Order) [33, 34]: This generator was used to simulate the $t\bar{t}$ events, and is a NLO generator. MC@NLO makes use of the HERWIG and Jimmy event generators and the events were NLO. Each background was weighted, (usually to $1fb^{-1}$) according to cross-section to match the signal. The PDF set used was CTEQ6M [31]
- ALPGEN [35]: This NLO generator also make use of HERWIG and Jimmy, and was used to simulate the $W + Jets$, $Z + Jets$, and QCD events. It is designed to simulate events with a large jet multiplicity. This produces a number of different samples for each background with different cross sections for a single background. In these cases the separate samples were weighted (usually to $1fb^{-1}$) according to their cross-section and recombined to make the single background. Again the PDF set used was

CTEQ6LI

2. Simulation of detector response: In this step the particles produced in the event generation have their interaction with the material in the detector, such as ionisation and showering, modelled. This process is carried out by GEANT4 [36, 37] and involves a full description of the magnetic field and materials in the detector.

The event reconstruction involves taking 'hits' and energy depositions in the detector, and using algorithms to reconstruct particles with their energy, position and identification. This is discussed later in this chapter.

3.2 ATLAS software

Athena [38, 27] is the name given to the ATLAS software. Whilst the course of this thesis involved using many different versions of Athena, the work was repeated in the latest available release, and all results presented here use version 14.2.20.

Athena is an object orientated C++ framework developed by ATLAS collaborators. Once the data has been simulated, it is stored as objects (in the sense of C++ objects) containing information about the event such as particle track parameters, or energy. Athena includes an event loop which allows for the data to be looped over on an event by event basis, accessing the stored information.

3.3 Object definitions

The ATLAS detector has various methods of detecting particles. The event reconstruction (for simulation or real data) takes the 'hits' and energy depostions of the detector and reconstructs them to form particles and jets. As discussed these are stored as C++ objects with the associated information stored with them. This is necessary for a physics analysis as the huge amount of information that the ATLAS detector produces needs to be classified into physical entities like electrons, muons and jets.

Below is a brief guide to the requirements that must be satisfied for these objects (electrons, muons and jets) to be created.

Electrons

The typical signature of an electron at ATLAS consists of a track matched to electromagnetic showering. This is as far as an electron usually penetrates. An electron is said to have been detected and is used in the analysis if the following are met.

1. An energy deposition is found in the ECAL.
2. A track in found in the inner detector.
3. The track and the energy depostion match according to $\Delta\eta < 0.05$, $\Delta\phi < 0.1$, $E/P < 10$, where η is the pseudo rapidity, ϕ is the azimuthal angle, E is the energy and P the momentum.

Other considerations such as hadronic leakage (the fraction of energy in the HCAL compared to the ECAL), and lateral shower shape in the second

compartment of the ECAL are summed up into a flag on the AOD known as the isEM flag. This flag also contains information about the hits in various inner detector layers. More information about the cuts applied in this flag may be found in [27]. An electron is only added by the analysis code if it has $P_T > 20\ GeV$ and $|\eta| < 2.5$.

Jets

Good quality and efficient jet reconstruction is an important tool for physics analyses at ATLAS. The jet energy scale [39, 27] is the calibration from detector readout, to the final goal of reconstructing the partons momentum. Due to confinement with the strong force, quarks are never observed in isolation. As the strong force increases with distance, energy is stored as quarks separate. When this energy is larger than the energy need to produce $q\bar{q}$ pairs then new particles are produced and this process is repeated. This process is known as hadronisation. Subsequent decay of hadrons can happen.

Jets are predominantly reconstructed used the ATLAS calorimeter systems which were discussed in chapter 2. The algorithm used in this analysis is the Cone algorithm [27, 40]. The Cone algorithm is a geometric jet finder which operates using high E_T particles as a seed to find the jet. First, all particles are listed in decreasing P_T. If the object with the highest P_T is above the seed threshold, all objects within a cone of $\Delta R = \sqrt{\Delta\eta^2 + \Delta\phi^2} < 0.4$ where η is the pseudo rapidity, and ϕ is the azimuthal anlge, are combined with the seed. The seed is updated to the direction of the cone and the process repeated until the direction of the cone does not change anymore.

As such a cone jet is the collection of particles within $\Delta R < 0.4$ of the cone axis which is aligned with the 4 momentum of the jet. A jet is only added by the analysis code if it has $E_T > 20\ GeV$ and $|\eta| < 2.5$.

Muons

The ATLAS detector, and particularly the muon spectrometer, discussed in chapter 2, has been designed to provide clean and efficient muon identification and precise momentum measurement.

Muons traverse the entire detector and deposit energy in all of the ATLAS sub-systems. Therefore it is necessary to use multiple algorithms to reconstruct them. Whilst the full details of these algorithms are not given a summary follows.

1. A track in the muon spectrometer is found, and a rough measurement of the P_T of the track is made
2. A check that is originates at the interaction point is performed.
3. A track is found in the inner detector.
4. If the two tracks are thought to be from the same particle, then the tracks are combined. This is done by the STACO (STAtistical COmbination) [27, 41] method which obtains a chi squared value which reflects the degree of success of the fit.

Due to energy loss in the calorimeters the P_T of the track in the muon spectrometer will be less than that in the inner detector. This energy loss means that for muons with an energy less than $\sim 100\ GeV$ the inner detector

track is used to measure the muon P_T, whereas for muons with P_T greater than ~100 GeV the tracks in the spectrometer are used. The analysis code requires a muon to have $P_T > 15\ GeV$ and $|\eta| < 2.5$.

Overlap removal

It is possible than a particle could meet the criteria of more than one object, for example an electron and a jet. In these cases, an order of precedence is observed in the analysis code. Firstly, objects that satisfy the electron requirements are defined. The analysis code then searches for any jets meeting the jet requirements with the additional constraint that there must not be a pre-defined electron within $\Delta R < 0.4$ of the prospective jet. Finally the muons passing the muon requirements are defined if they are not inside a cone of $\Delta R < 0.4$ of a jet.

3.4 Summary

This chapter introduces the idea of simulating data to study possible physics scenarios using ATLAS. The ATLAS software and the object reconstruction are introduced. The generators used for the simulation listed, and the requirements for electrons, muons and jets were given. The next chapter takes a look at detector performance and particularly the measurement of E_T^{miss}.

Chapter 4

Missing Transverse Energy Measurement

4.1 Introduction

The ATLAS detector is capable of directly observing many particles such as electrons, muons, and jets of hadrons, although neutral particles that only interact via the weak force and which have a low interaction cross section, will usually pass through the detector without interacting. However, the 360 degree coverage in the transverse plane of the ATLAS detector allows for the presence of particles such as the neutrino or neutralino to be inferred by the imbalance they leave in the transverse momentum which should sum to zero. This imbalance depends on the calorimeter measurements and leads to the concept of missing transverse energy or E_T^{miss}.

An understanding of the detector performance in measuring E_T^{miss} is critical for a number of physics studies. Poor detector performance will produce

a positive E_T^{miss} even when all particles have interacted in the detector and been measured. E_T^{miss} is faked by

1. Finite detector resolution causing fluctuations away from zero. This is particularly true in the hadronic calorimeters as the resolution is worse than the electromagnetic calorimeters.

2. Particles escaping detection because of cracks, and inefficiencies, also particles outside of the acceptance of the detector.

Many physics analyses, such as those involving reconstructing the missing neutrinos from W's or tau's need a good understanding of this resolution. In particular, E_T^{miss} is the main variable used in an analysis investigating the existence of R-parity conserving SUSY as the LSP is mainly weakly interacting and stable. This motivates the following study of how accurately ATLAS can measure this quantity. A previous study may be found in [27].

4.2 Aim

This study investigates the use of early data to understand the relationship between the resolution of E_T^{miss} and the amount of energy deposited in the combined calorimeter. The resolution in the HCAL is $\sigma_E/E = 50\%/\sqrt{E} \oplus 3\%$ for the barrel and end-caps and the forward calorimeter has a resolution of $\sigma_E/E = 100\%/\sqrt{E} \oplus 10\%$ (see chapter 2). Therefore, it is expected that larger energy depositions (especially in the hadronic calorimeter) will increase the error in the measurement of $E_T^{miss}$and result in a wider resolution.

The idea is to use events in which the real E_T^{miss} is expected to be small,

Alpgen Samples

Sample	Cross Section pb	Number of events generated
$Z \rightarrow e^+e^-$ 0 partons	1096.1	2.5×10^5
$Z \rightarrow e^+e^-$ 1 partons	241.3	6.0×10^4
$Z \rightarrow e^+e^-$ 2 partons	76.0	1.8×10^5
$Z \rightarrow e^+e^-$ 3 partons	22.9	5.6×10^4
$Z \rightarrow e^+e^-$ 4 partons	6.1	1.5×10^4
$Z \rightarrow e^+e^-$ 5 partons	1.7	4.5×10^3

Table 4.1: A table showing the samples of $Z \rightarrow e^+e^- + Jets$ used, cross section and number generated

have a high enough cross-section so as to be plentiful in the early data and which can be cleanly identified. The $Z \rightarrow e^+e^- + Jets$ channel satisfies these requirements. In the absence of real data, the study is performed using full Monte Carlo simulations of collisions. The number of events and cross section produced is shown in table 4.1. Events are selected by requiring two oppositely charged 'electrons', with a reconstructed mass between 70-100GeV. The E_T^{miss} due to neutrinos is expected to be negligible. Figure 4.1 shows the E_T^{miss} truth for events in the sample and shows that it is small. However, possible backgrounds are $Z \rightarrow \tau\tau$, $W \rightarrow l\nu$, and di-jet events in which two leptons are falsely identified. The first two of these backgrounds are expected to be small [27] but will have to be studied. The jet background will have to be evaluated when real data is present because it is difficult to generate enough events. The processes which lead to jets faking electrons are very rare - it is only the huge cross-section which makes them a problem.

Figure 4.2 shows the number of identified electrons, whilst figure 4.3 shows the number of reconstructed jets in each event. The requirements for these identifications was as set out in chapter 3. Figure 4.2 shows a maximum of

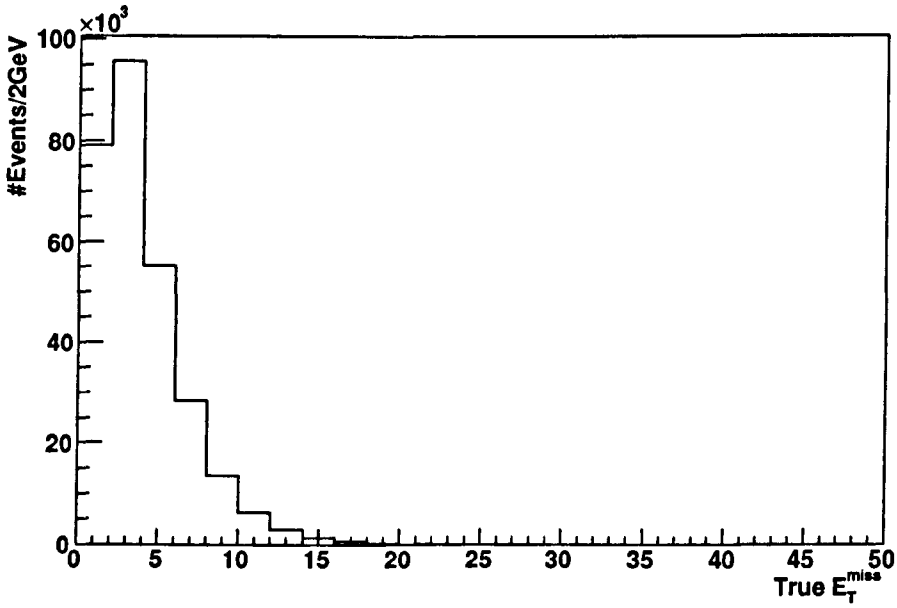

Figure 4.1: True E_T^{miss} in each event

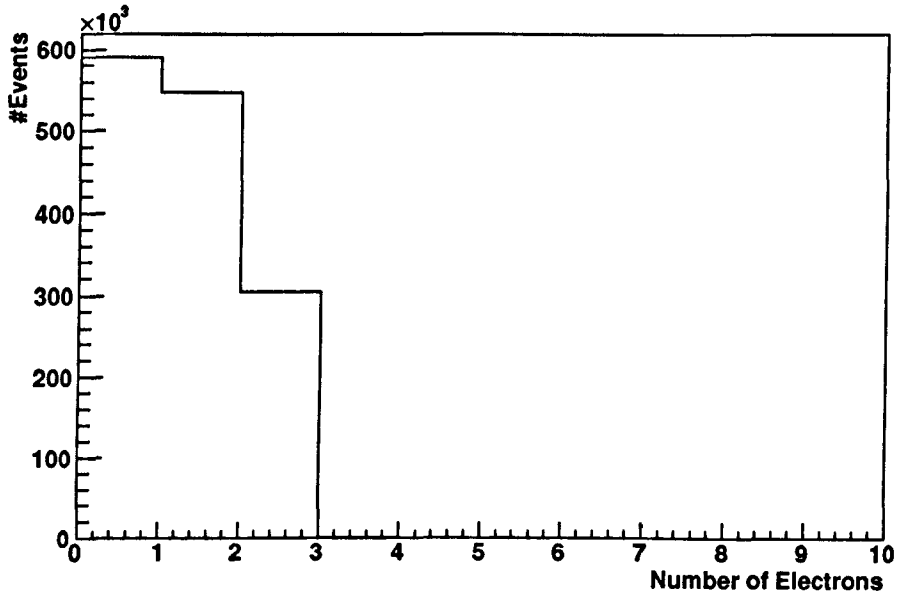

Figure 4.2: Number of identified electrons with $P_T > 20GeV$

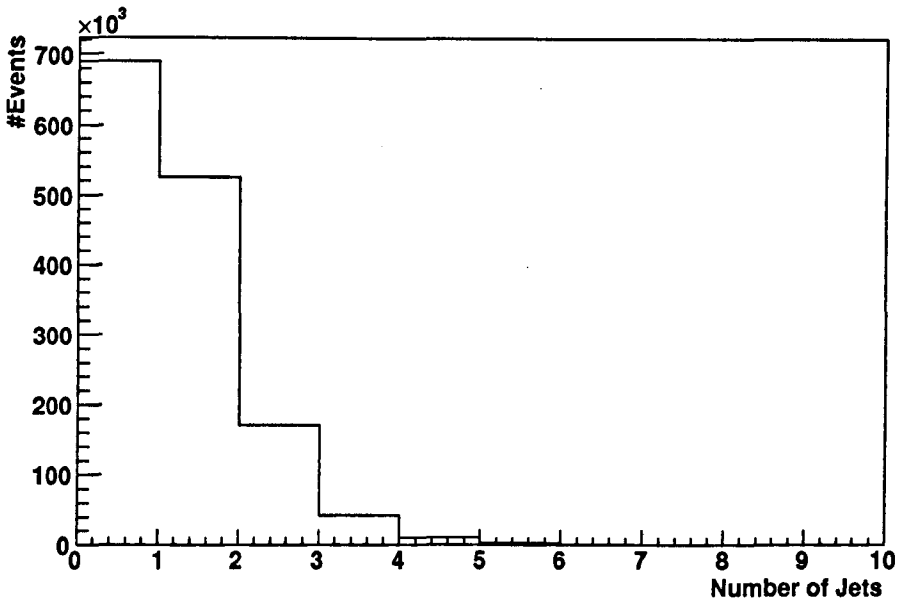

Figure 4.3: Number of reconstructed jets of hadrons

2 electrons in an event. For the cases where we have less than two electrons, one or both of the electrons have been produced outside of the acceptance of the detector or misidentified.

Figure 4.4 shows the P_T of electrons identified in each event. The electrons must have a $P_T > 20\ GeV$, there must be exactly two of them, they must have an invariant mass of greater than 70 GeV and less than 100 GeV., and they must be oppositely charged. The peak corresponds to roughly half the Z mass which results from a Z decaying to two particles, and as θ of the electrons varies, so too does their P_T.

Figure 4.5 shows the P_T of jets of hadrons in selected events in which a Z boson has been identified

The plots in Figure 4.6 were made for events in which exactly two elec-

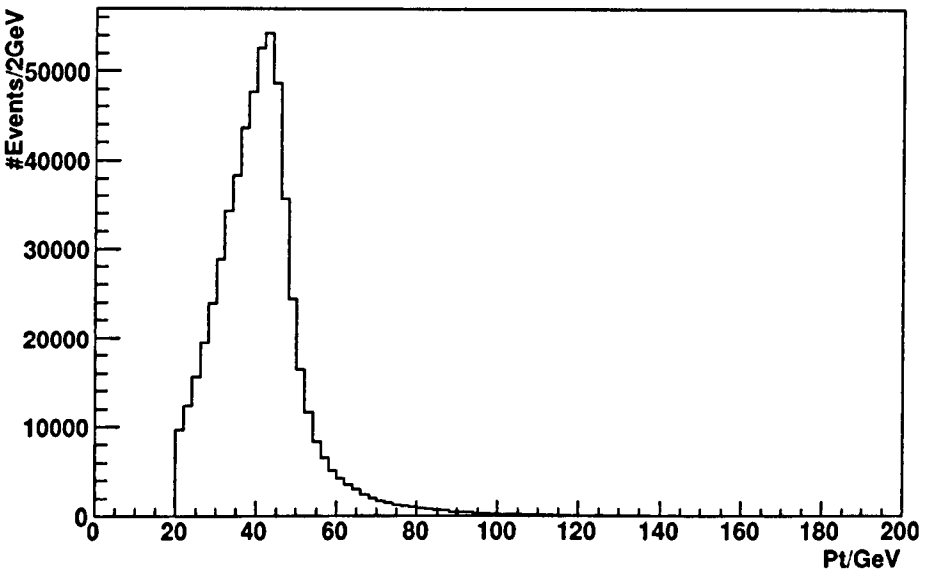

Figure 4.4: P_T of electrons requiring exactly 2 'electrons' with invariant mass greater than 70GeV and less than 100GeV

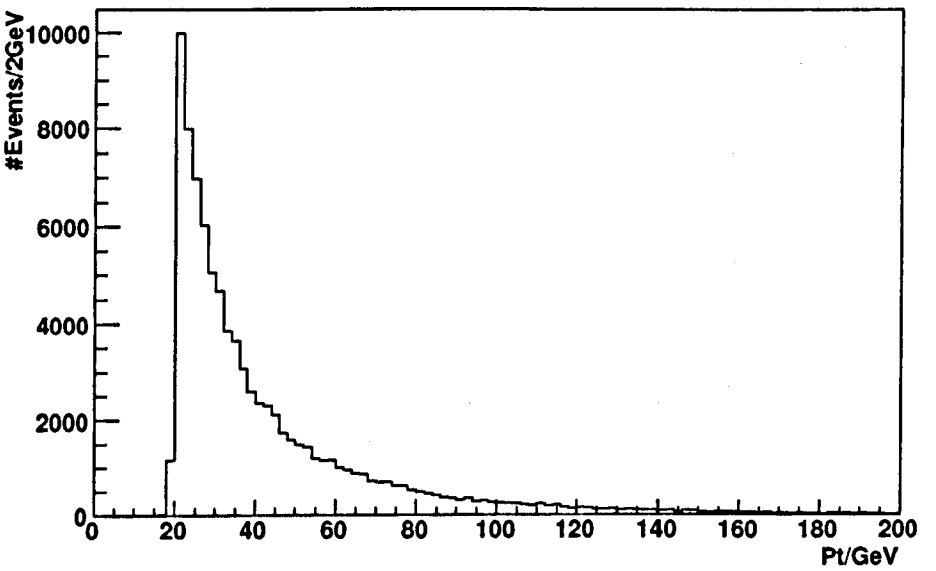

Figure 4.5: P_T of jets of hadrons in each event containing exactly two 'electrons' with invariant mass greater than 70GeV and less than 100GeV

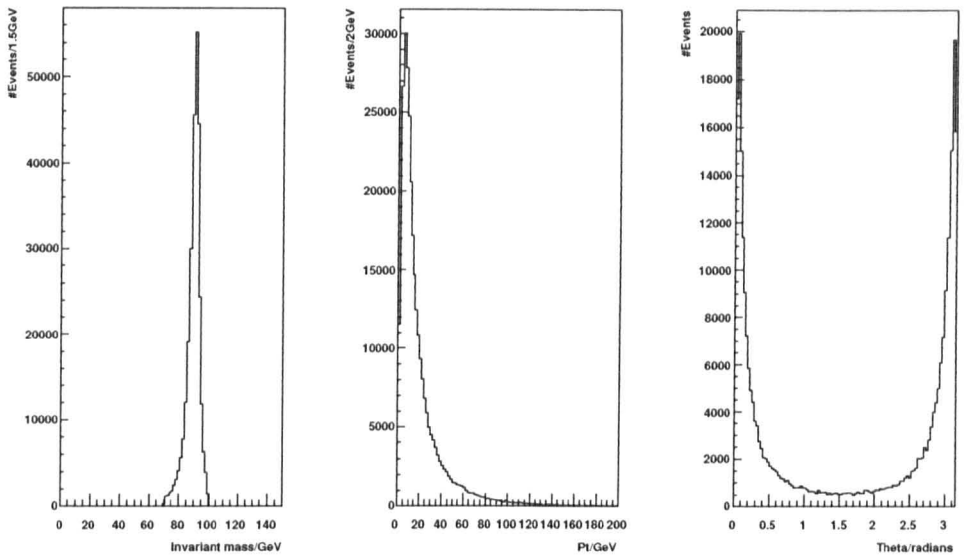

Figure 4.6: Plots of the mass, P_T, and θ of the reconstructed Z

trons were reconstructed. The electrons passed the criteria set out in chapter 3. The plot of the invariant mass (left) shows a peak at the Z mass which confirms the electrons are the decay products of a Z. The plot of the P_T of the Z candidate (middle) shows that it typically has low P_T. The final plot showing theta of the Z candidate shows that the Z predominantly travels along the beam direction.

4.3 Minimising the effect of the Electrons on the E_T^{miss} resolution

The aim is to investigate the fake E_T^{miss} resulting from the uncertainties in measuring the hadronic energy. This study takes the resolution of a compo-

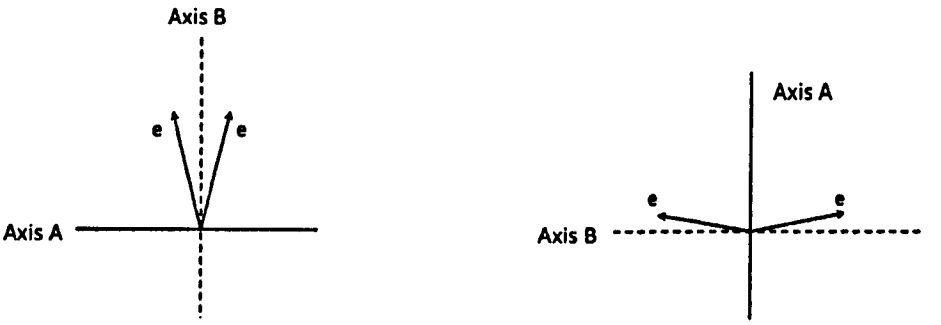

Figure 4.7: Diagrams showing the 2 axes A and B defined in the text for the 2 possible configurations of electrons in the transverse plane

nent of the E_T^{miss} and parametrises it with the total hadronic energy component that caused it. In the $Z \rightarrow e^+e^- + Jets$ channel, the E_T^{miss} will be due to the mis-reconstruction of the jets and electrons. Investigating the performance of the calorimetry in measuring hadrons requires the resolution effects in the measurement of the electrons be minimised. This is achieved by selecting an axis along which the component of the sum of the electron momenta is a minimum. Along this axis, the contribution to the component of E_T^{miss} due the electron resolution will also be a minimum.

Consider the two diagrams in figure 4.7 in which there are 2 hypothetical electrons in the x-y plane. The A axis is constructed by taking the vector bisecting the two electrons for the case where $\Delta\phi$ between the electrons is greater than 90°and taking the vector perpendicular to this if $\Delta\phi$ between the electrons is less than 90° . The B axis is a rotation of the A axis by 90°. The component of the momenta of the electrons along the A axis is less than the component along the B axis. (The axes are defined this way because the

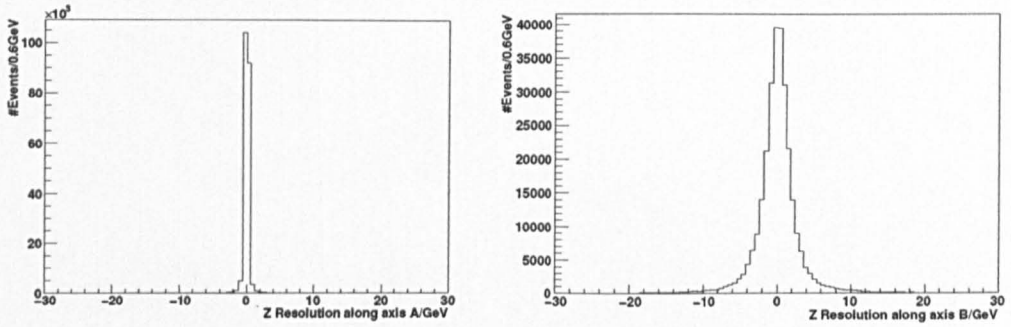

Figure 4.8: Z momentum component along Axis A (left) and Axis B (right)

ATLAS detector measures angles better than energy, hence the resolution of the electron momenta along axis A is at a minimum.) Figure 4.8 shows the true 'Z' momenta component minus the measured 'Z' momenta component resolved along axis A (left) and B (right). It can be seen that the width of this resolution curve for axis A (3GeV) is narrower than that for axis B (8 GeV). For the rest of this study axis A will be used.

4.4 Understanding the resolution

Having chosen an axis which minimises the resolution effects caused by the electrons, and using a channel in which there is little real E_T^{miss}, it is assumed that the E_T^{miss} along this axis is solely due to mis-measurement in the combined calorimetry, mainly the HCAL.

More specifically, as only a component of E_T^{miss} is being considered, it is the mis-measurement of the hadronic energy (along the same axis) that causes this E_T^{miss}. Contributions to the fake E_T^{miss} along this axis will come from all the individual energy measurements multiplied by the cosine of the

angle to this axis. To investigate this, the component of the hadronic energy was calculated using the formula below.

$$E_{Axis} = \sum |E_{TClusters}| \times \frac{\sum_i |E_{TJet_i} \times cos\phi_i|}{\sum_i |E_{TJet_i}|} \tag{4.1}$$

where ϕ is the angle between the jet and axis A. This quantity is used, as whilst the sum of the hadronic calorimeter energy includes information on a per cell basis, it is a scalar and thus does not have direction and a component cannot be taken. Multiplying by the fraction of the jet energy along the axis being considered gives us the needed directional information.

The component (along the A axis) of E_T^{miss} was plotted against the component (also along the A axis) of resolved hadronic energy as calculated in equation 4.1 and it is shown in figure 4.9.

Figure 4.9 was divided along the x axis into 20 vertical slices of width 25 GeV. The first three distributions of E_T^{miss}in each slice are shown on a log scale in figure 4.10 with P_T increasing down the page.

The distributions are approximately Gaussian, and so Gaussian curves were fitted to the data in each slice. The fits are shown superimposed on the data in blue on figure 4.10.

Figure 4.11 shows how the width of these Gaussian fits varied with total hadronic energy component.

This plot has been fitted with the function $a \times x^b + c$ and the fit is drawn on the plot. The parameters from the fit were

$a = 0.02 \pm 0.005$

$b = 0.95 \pm 0.04$

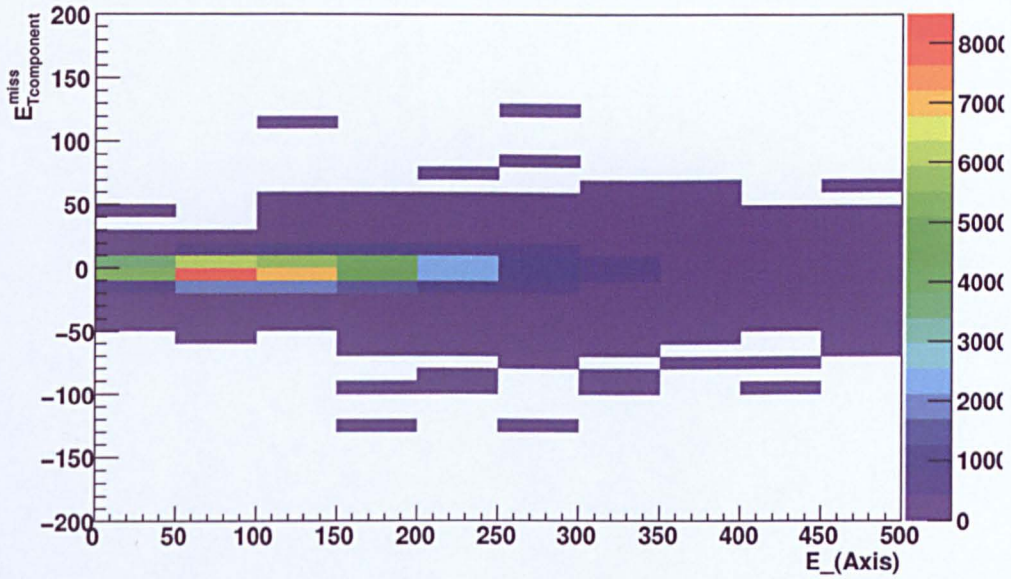

Figure 4.9: The E_T^{miss} component resolved on Axis A, as a function of total hadronic energy component along the same axis

$c = 5.02 \pm 0.07$

This formula can then be used to measure the resolution on E_T^{miss}. x may be calculated by choosing the axis to be the axis of the E_T^{miss} vector.

In conclusion the $Z \rightarrow e^+e^- + Jets$ channel can be used to study the performance of ATLAS in measuring E_T^{miss} and obtain a parametrisation for the resolution in this parameter.

4.5 Summary

In this chapter the $Z \rightarrow e^+e^- + Jets$ channel was investigated to determine how it might be used to determine the resolution of E_T^{miss} in early data. Real E_T^{miss} in these events was minimised, and the effect of the electron

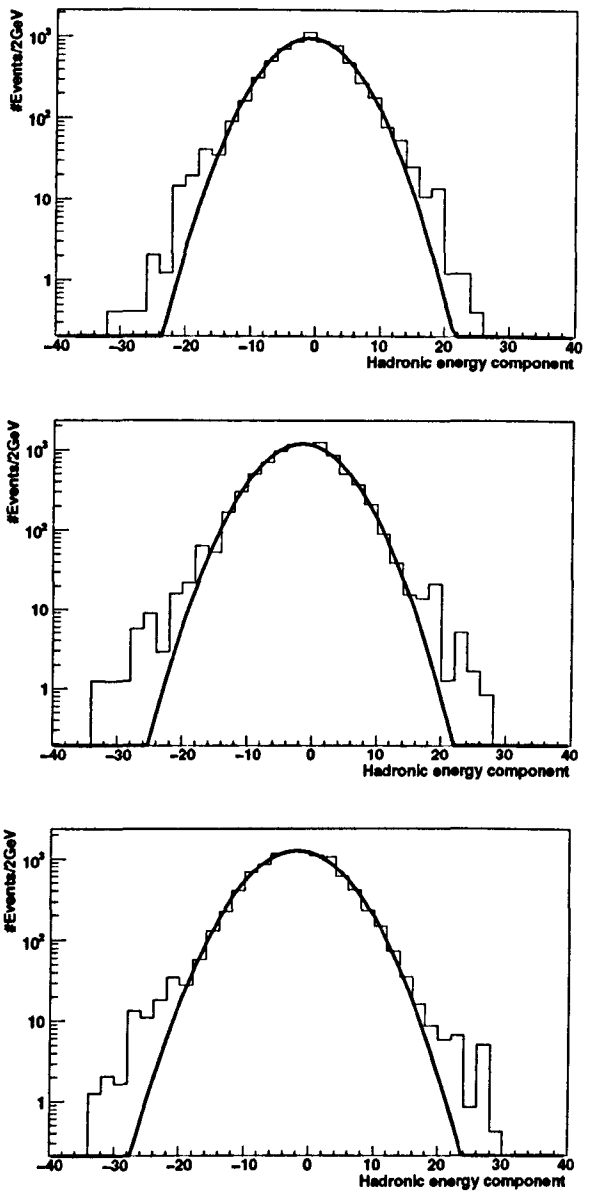

Figure 4.10: The first three slices showing resolution in each plot as a function of the hadronic energy component. Gaussian curves have been fitted to the data and are shown on the plots P_T increases down the page. The complete set of slices is shown in the appendix.

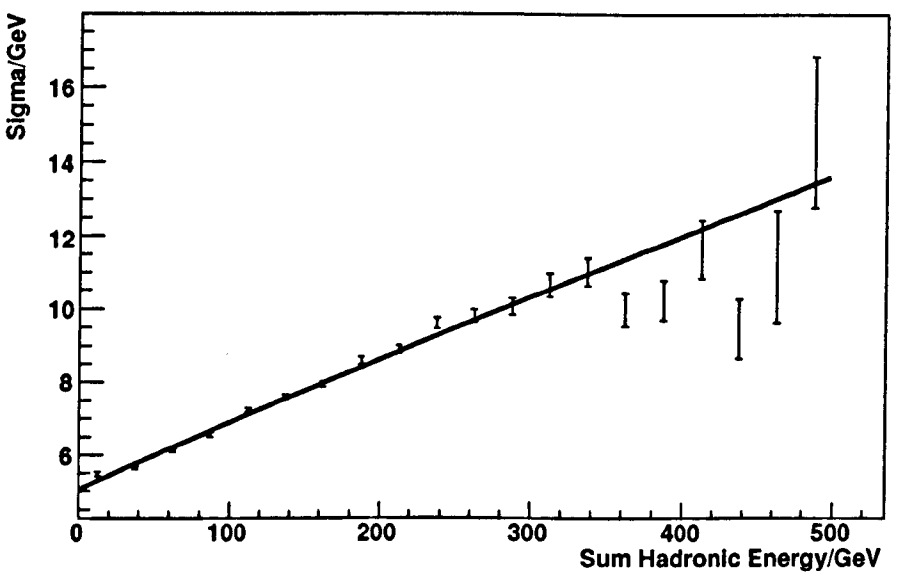

Figure 4.11: A graph showing the sigmas (where each sigma is the width of a gaussian fit to a particular slice) of the fits to each slice against component of hadronic energy. The solid line is the parametrisation described in the text.

measurements on the resolution was also minimised. The assumption was made that the E_T^{miss} resolved onto a certain axis (see section 4.3) was the resolution. It was shown how this data could be used to determine the resolution along this axis. This resolution was parametrised.

Chapter 5

Optimisation of Event Selection for mSugra based SUSY searches

In this chapter the optimal procedure for performing an mSugra SUSY search with zero leptons in the final state is investigated. Events at different mSugra points can be qualitatively different due to different particle masses and different decay chains. The best selection procedure may therefore be dependent on the mSugra parameters. This is investigated in this chapter. Firstly, the simulated data and the background used are discussed. Then an earlier ATLAS study [27] is repeated with the data, and the resulting significances calculated for a range of points in mSugra parameter space. The next steps are to investigate two approaches to optimise the selection for the range of points. The first method seeks the optimal set of orthogonal cuts on the variables, while the second applies a log likelihood technique to the same same set of variables. The significance (see section 5.5.1) of these two methods are compared with each other and with the earlier ATLAS study, and a

discussion follows.

All of the data used in this analysis has been generated with a full simulation of the detector. Object selection was as described in chapter 3, and the ALPGEN samples were combined according to cross section for the individual samples and scaled for $1fb^{-1}$ as described in chapter 3.

5.1 Signal

For the purpose of this analysis a set of five SUSY points in the mSugra framework were chosen to investigate the potential for early discovery at the LHC. The chosen points are consistent with the observed density of cold dark matter and beyond current limits obtained at the Tevatron. They are designed to be representative of the SUSY regions accessible with relatively early data. The points investigated are defined by the following mSugra parameters:

1. "SU1": $m_0 = 70\,GeV$, $m_{\frac{1}{2}} = 350\,GeV$, $A_0 = 0$, $tan\beta = 10$, $\mu > 0$.
2. "SU3": $m_0 = 100\,GeV$, $m_{\frac{1}{2}} = 300\,GeV$, $A_0 = -300$, $tan\beta = 6$, $\mu > 0$.
3. "SU4": $m_0 = 200\,GeV$, $m_{\frac{1}{2}} = 160\,GeV$, $A_0 = -400$, $tan\beta = 10$, $\mu > 0$.
4. "SU6": $m_0 = 320\,GeV$, $m_{\frac{1}{2}} = 375\,GeV$, $A_0 = 0$, $tan\beta = 50$, $\mu > 0$.
5. "SU8.1": $m_0 = 210\,GeV$, $m_{\frac{1}{2}} = 360\,GeV$, $A_0 = 0$, $tan\beta = 40$, $\mu > 0$.

Label	$\sigma(pb)$ at 10TeV	No. of events generated
SU1	2.42	10000
SU3	5.46	10000
SU4	107.4	49217
SU6	1.23	8221
SU8.1	1.79	8466

Table 5.1: A table showing the cross sections (σ) (at 10 TeV) of the Monte Carlo SUSY points used for this analysis.

The points were generated for a proton-proton collision with centre of mass energy of 10 TeV, and the cross-sections at this energy are shown in table 5.1. The main production cross-sections at the LHC for the points being studied in this analysis lead to the production of gluino and squark pairs decaying to $\tilde{\chi}_1^0$s. The decay from gluinos and squarks to the $\tilde{\chi}_1^0$ takes place via several steps and a typical decay chain is shown below.

$$\tilde{g} \rightarrow \tilde{q}_L\bar{q} \rightarrow \tilde{\chi}_2^0 q\bar{q} \rightarrow \tilde{\chi}_1^0 \tilde{l}^{\pm}\tilde{l}^{\pm} q\bar{q} \rightarrow \tilde{\chi}_1^0 l^+ l^- q\bar{q}$$

The gluino ($\tilde{g}$) decays to a left handed squark ($\tilde{q_L}$) even when it cannot decay to the right handed squark as it is lighter. From the decay chain we can infer the general features that will be detected if super-symmetric particles are being produced at the LHC. The following signatures should be expected.

- Large number of high P_T jets. This is due to the long length of the decay chain and the large P_T difference between decay products of the decay chain.

- A large fraction of the energy will escape interaction in the detector and be observed as an imbalance of transverse energy. This is because

the energetic $\tilde{\chi}_1^0$ only interacts via the weak force and will not interact in the detector.

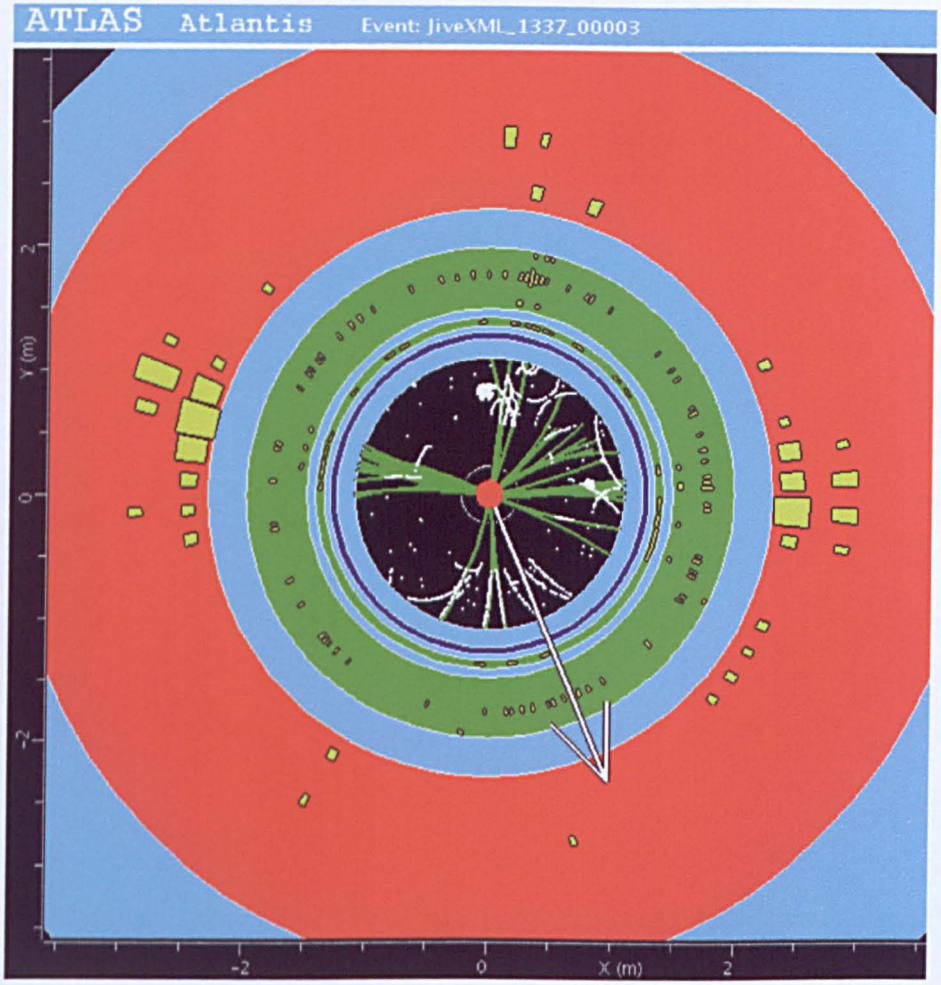

Figure 5.1: A reconstructed mSugra style event at the LHC

Figure 5.1 shows a reconstructed mSugra event at the LHC. The white arrow shows the direction of the E_T^{miss} vector, and a number of hadronic jets may be observed as yellow energy deposits in the HCAL.

5.2 Backgrounds

The major backgrounds from the Standard Model are Z + Jets, W + jets, $t\bar{t}$, and jet production from QCD processes. Many of these backgrounds have a high jet multiplicity, similar to the SUSY events, and will also leave an imbalance in the detection of transverse energy either through the presence of weakly interacting neutrinos that exit the detector without interacting, or due to mismeasurement of the large number of jets.

W+Jets

Alpgen Samples

Sample	Cross Section (pb)	Number of events generated
$W \rightarrow e + \nu$ 0 partons	12208.0	3.0×10^5
$W \rightarrow e + \nu$ 1 partons	2444.3	6.0×10^5
$W \rightarrow e + \nu$ 2 partons	760.4	1.5×10^5
$W \rightarrow e + \nu$ 3 partons	218.4	4.5×10^4
$W \rightarrow e + \nu$ 4 partons	56.8	1.0×10^4
$W \rightarrow e + \nu$ 5 partons	16.5	3.3×10^3
$W \rightarrow \mu + \nu$ 0 partons	12475.9	3.0×10^5
$W \rightarrow \mu + \nu$ 1 partons	2461.3	5.5×10^4
$W \rightarrow \mu + \nu$ 2 partons	763.4	1.5×10^5
$W \rightarrow \mu + \nu$ 3 partons	210.4	2.4×10^4
$W \rightarrow \mu + \nu$ 4 partons	57.1	1.2×10^4
$W \rightarrow \mu + \nu$ 5 partons	16.3	3.0×10^3

Table 5.2: A table showing samples of $W \rightarrow l\nu + Jets$ used, cross section and number generated

W+Jets is a background for SUSY events as the W can decay to a lepton and a neutrino which then leaves the detector leading to E_T^{miss}. A lepton veto reduces this background significantly. It is worth pointing out that the

$W \rightarrow \tau + \nu$ sample (where the τ decays hadronically) has not been included however it is included in the previous study[27].

Z +Jets

Alpgen Samples

Sample	Cross Section pb	Number of events generated
$Z \rightarrow e^+e^-$ 0 partons	1096.1	2.5×10^5
$Z \rightarrow e^+e^-$ 1 partons	241.3	6.0×10^4
$Z \rightarrow e^+e^-$ 2 partons	76.0	1.8×10^5
$Z \rightarrow e^+e^-$ 3 partons	22.9	5.6×10^4
$Z \rightarrow e^+e^-$ 4 partons	6.1	1.5×10^4
$Z \rightarrow e^+e^-$ 5 partons	1.7	4.5×10^3
$Z \rightarrow \mu^+\mu^-$ 0 partons	1092.2	2.7×10^5
$Z \rightarrow \mu^+\mu^-$ 1 partons	242.3	6.0×10^4
$Z \rightarrow \mu^+\mu^-$ 2 partons	77.5	1.9×10^5
$Z \rightarrow \mu^+\mu^-$ 3 partons	22.8	5.6×10^4
$Z \rightarrow \mu^+\mu^-$ 4 partons	6.1	1.4×10^4
$Z \rightarrow \mu^+\mu^-$ 5 partons	1.6	4.2×10^3
Pythia sample		
$Z \rightarrow \nu\nu$	3528	986214

Table 5.3: A table showing samples of $Z \rightarrow l^+l^- + Jets$ used, cross section and number generated

In these events the Z boson can decay to charged leptons via: $Z \rightarrow l^+l^- + jets$ with the high number of jets creating fake E_T^{miss} as discussed in chapter 4. Another further background which has not been included in this study is $Z \rightarrow \tau^+\tau^- + Jets$ however it was included in the previous study [27]. The Z can also decay to neutrinos via: $Z \rightarrow \nu\tilde{\nu}$. Here, the combination of the high number of jets and the real E_T^{miss} due to the weakly interacting particles cause a background.

$t\bar{t}$

MC@NLO Samples

Sample	Cross Section pb	Number of events generated
$t\bar{t}$ Full hadronic	208.3	9.9×10^4
$t\bar{t}$	217.1	1.6×10^5

Table 5.4: A table showing samples of $t\bar{t}$ used, cross section and number generated

The t decays via: $t \rightarrow Wb$ with the W decaying either by $W \rightarrow l\nu$ (the sample shown in table 5.4 labelled as '$t\bar{t}$' has at least one of the tops decaying leptonically in this way) which gives real E_T^{miss} but may be significantly removed via a lepton veto, or $W \rightarrow q\bar{q}$ (the sample shown in table 5.4 as '$t\bar{t}$ full hadronic' is for the case where both tops decay to quarks in this way) which only gives fake E_T^{miss} .

Jet production from QCD processes

Alpgen samples

Sample	Cross Section pb	Number of events generated
QCD 0 partons	1.2×10^{10}	3.9×10^5
QCD 1 partons	8.7×10^8	3.9×10^5
QCD 2 partons	5.6×10^7	8.2×10^4
QCD 3 partons	3.2×10^6	4.0×10^5
QCD 4 partons	1.5×10^5	3.7×10^5
QCD 5 partons	5.2×10^3	3.9×10^5
QCD 6 partons	112	3.9×10^5

Table 5.5: A table showing samples of QCD used, cross section and number generated

QCD events have a very large cross section and generate a large number of jets which through mis-measurement cause fake E_T^{miss}.

5.3 Global Variables

The aim of this analysis is to optimise selections using variables that will discriminate SUSY from Standard Model processes so that a potential signal may be identified. SUSY events have large real E_T^{miss} and numerous high P_T jets that may be used to discriminate them from the Standard Model processes. In this section, the variables used in this analysis are presented.

The huge QCD background may be largely reduced by simple preselection cuts. The preselection cuts for this analysis are:

1. $E_T^{miss} > 50\ GeV$
2. At least 1 hadronic jet $P_T > 20\ GeV$
3. 0 electrons with $P_T > 20\ GeV$
4. 0 muons with $P_T > 20\ GeV$

The analysis framework, overlap removal and object selection was as outlined in chapter 3. All of the distributions are plotted for an integrated luminosity of 1 fb^{-1}. Figures 5.2, 5.3, 5.4, 5.5, 5.6, 5.11, and 5.12 show the signal (SU3 is used as an example) in red, the ttbar background in black, the $W \rightarrow l + \nu$ background in blue, the $Z \rightarrow l + l$ background in green, the QCD background in yellow and the $Z \rightarrow \nu\nu$ background in purple.

5.3.1 Missing Transverse Energy

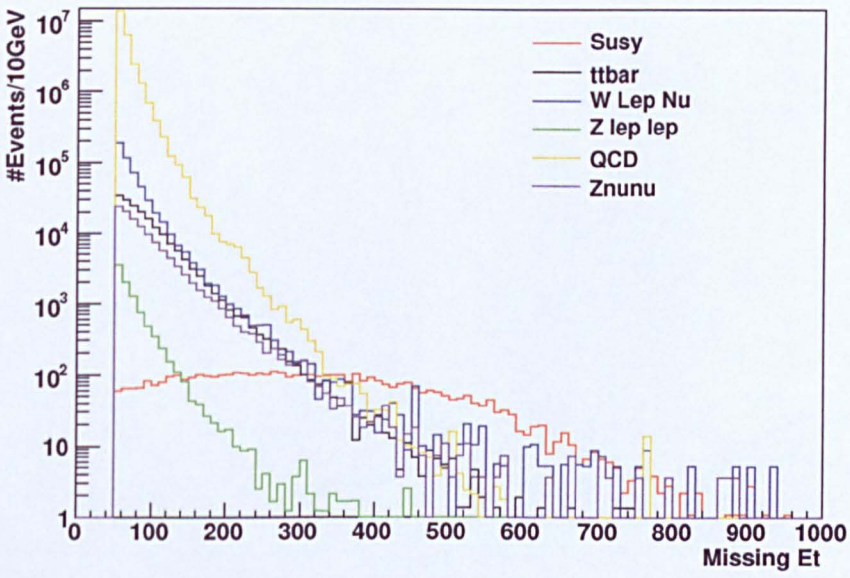

Figure 5.2: The E_T^{miss} variable for SU3 and the SM backgrounds once the preselection has been applied.

As discussed in chapter 4, the presence of particles which cannot be detected, such as neutrinos and the massive LSP (lightest Super-symmetric particle) may be inferred by noticing an imbalance in the transverse energy. Figure 5.2 shows a histogram of the missing transverse energy for the signal sample and for each of the backgrounds.

5.3.2 Number of Jets with Transverse Momentum Greater than 50 GeV

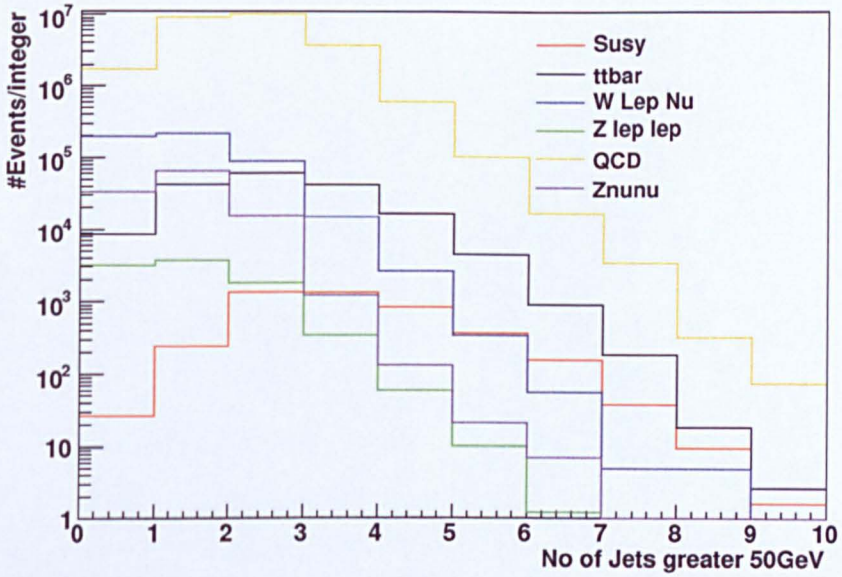

Figure 5.3: The number of cone jets with P_T> 50 GeV. The preselections of $E_T^{miss} > 50\ GeV$ and Number of $P_T > 8\ GeV$ jets > 1 were applied.

SUSY events have jets with high P_T. This is because of the large mass of the squarks or gluinos initially produced. Figure 5.3 shows the number of jets with $P_T > 50\ GeV$ for the (SU3) signal and the backgrounds.

5.3.3 Transverse Momentum of Lead Jet

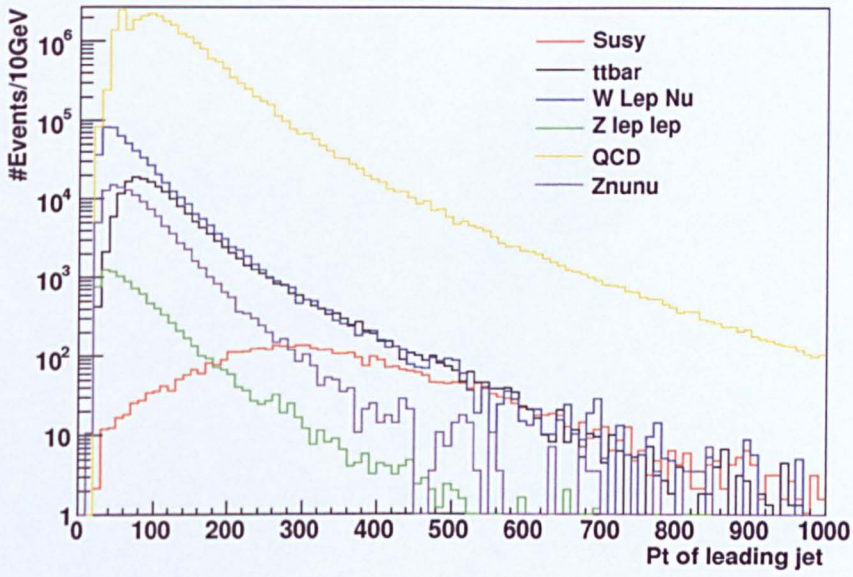

Figure 5.4: The P_T of the lead jet

When the high mass squarks and gluinos produced at ATLAS decay, the resulting jets will have a high P_T, especially the lead jet. The jets in the backgrounds tend to have a much lower P_T because they are produced when a particle with a lower mass decays. To further reduce the background we can put a selection on the P_T of the lead jet. Figure 5.4 shows the P_T of the lead jet for each event including both the (SU3) signal and the backgrounds.

5.3.4 Transverse Sphericity

The transverse sphericity S_T is defined as:

$$S_T \equiv \frac{2\lambda}{(\lambda_1 + \lambda_2)}$$

λ_1 and λ_2 are the eigenvalues of the 2x2 sphericity tensor, $S_{ij} = \sum_k p_{ki} p^{kj}$ and p is the momentum transverse to the beam. λ is the smallest eigenvalue. All identified jets and leptons are used to calculate S_{ij}.

This variable was investigated for distinguishing between QCD events and SUSY events, as for SUSY the squarks and gluinos are produced roughly at rest and the decay products travel in many different directions. This produces a high S_T. QCD events on the other hand are predominantly di-jet events and as such should have a S_T closer to 0.

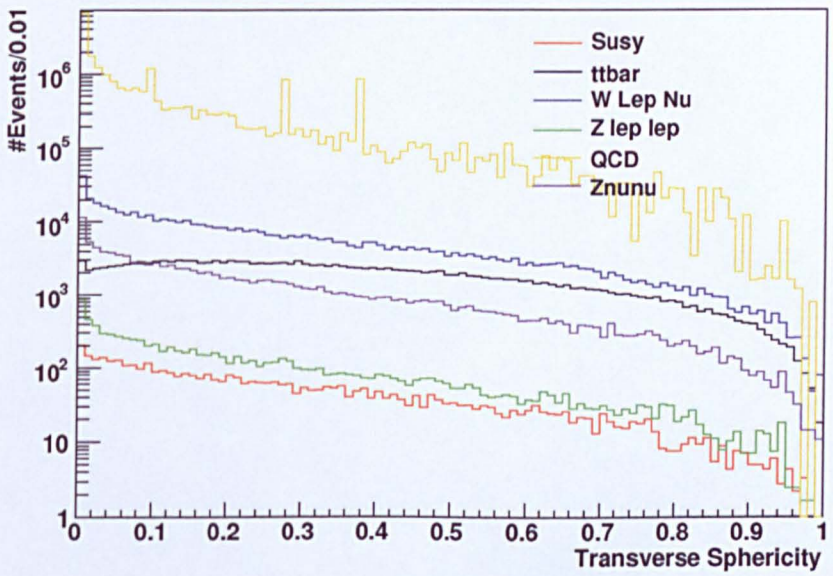

Figure 5.5: The transverse sphericity

Figure 5.5 shows the transverse sphericity for the (SU3) SUSY sample and for the backgrounds. The spikes in the QCD background distribution are due to 3 spurious 2-parton events which passed the pre-selection cuts (and carried enormous weights because of the very high cross-section for these processes).

5.3.5 Effective Mass

The scalar quantity effective mass (M_{eff}) is used in this analysis and is proportional to m_0, $m_{\frac{1}{2}}$ [27]. The definition is:

$$M_{eff} \equiv \sum_{i=1}^{4} p_t^{jet,i} + \sum_{i=1} p_t^{lep,i} + E_T^{miss}$$

which is the sum of the P_T of the four jets with highest P_T, P_T of identified leptons and missing transverse energy.

5.4 ATLAS study selections

In order to benchmark the analysis, the selections from an earlier ATLAS study [27] were repeated. The selections for the study are as follows:

1. At least four jets with $P_T > 50$ GeV at least one of which must have $P_T > 100\ GeV$; and $E_T^{miss} > 100\ GeV$.
2. $E_T^{miss} > 0.2$ Effective mass
3. Transverse Sphericity >0.2
4. $\Delta\phi(jet_1 - E_T^{miss}) > 0.2, \Delta\phi(jet_2 - E_T^{miss}) > 0.2, \Delta\phi(jet_3 - E_T^{miss}) > 0.2$
5. Reject events with an e or a μ with P_T greater than 10 GeV
6. Effective Mass > 800 GeV

The plots in figure 5.6 show how the effective mass varies as the above cuts are applied. The significance (see section 5.5.1) as a function of a cut on effective mass is also shown.

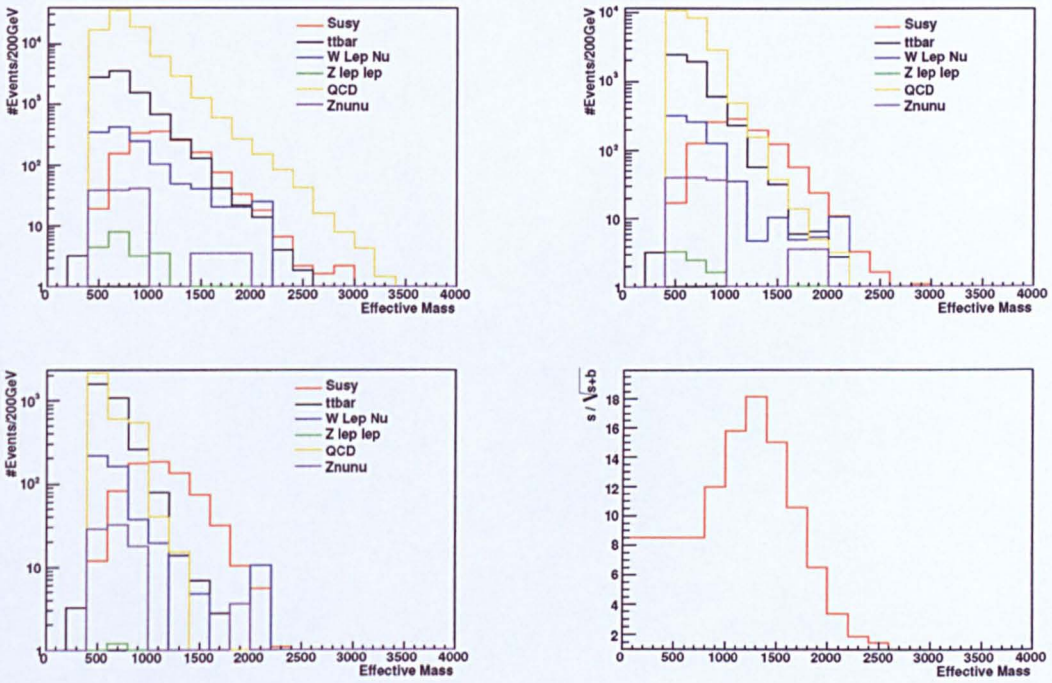

Figure 5.6: Effective Mass plots with successive cuts. The plot on the top left shows after cut 1, top right shows after cut 1 and 2, and the bottom left shows after cuts from 1 to 5. The plots show the signal and each Standard Model background. The plot in the bottom right shows the dependence of the significance on the value of the a cut on effective mass after cuts 1-5.

5.5 Optimising Selections for the individual SUSY scenarios

In order to find a near optimal combination of cuts on the 4 variables considered in section 5.3, each was independently varied in fixed increments, and for all possible combinations of these cuts the number of signal and background events were recorded. The results for the SU3 sample are shown in figure 5.7. It can be seen in these plots that as the cuts are hardened, the

background tends to decrease faster than the signal.

N	$N_1(> E_T^{miss}/GeV)$	$N_2(\geq$# jets with $P_T > 50GeV$	$N_3(> P_T$ lead jet)	$N_4(>S_T)$
0	0	0	0	0
1	50	1	50	0.01
2	100	2	100	0.02
3	150	3	150	0.03
4	200	4	200	0.04
5	250	5	250	0.05
6	300	6	300	0.06
7	350	7	350	0.07
8	400	8	400	0.08
9	450	9	450	0.09

Table 5.6: Table showing the value of the cut on each variable

Table 5.6 shows the values of each of the cuts considered. The cuts are labelled with an integer (0-9) and the abscissa in the plots in figure 5.7 is given by

$$Cut\ \ number = N_1 \times 1000 + N_2 \times 100 + N_3 \times 10 + N_4 \times 1$$

Where N_1 labels the cut on E_T^{miss}, N_2 labels the cut on number of jets with $P_T > 50\ GeV$, N_3 labels the cut on P_T of the lead jet, and N_4 labels the cut on S_T.

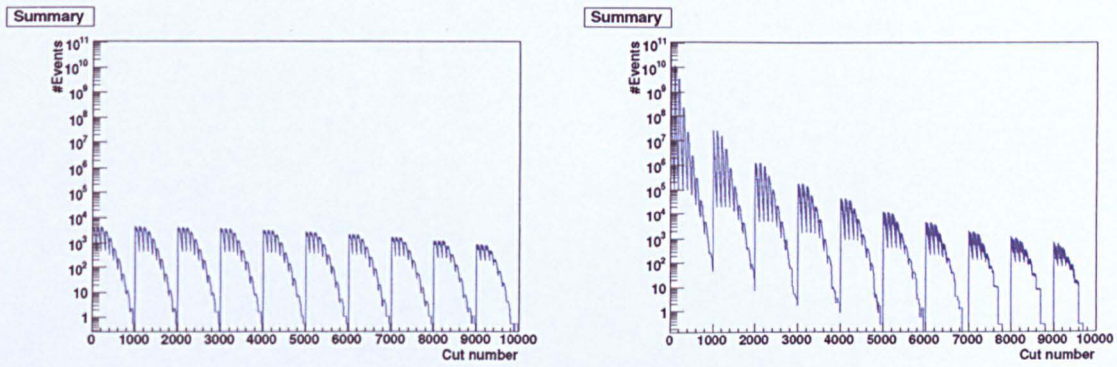

Figure 5.7: Plots showing the number of signal events (left) with SU3 as the example used and background events (right) that passed each set of cuts. The x axis is as described in the text

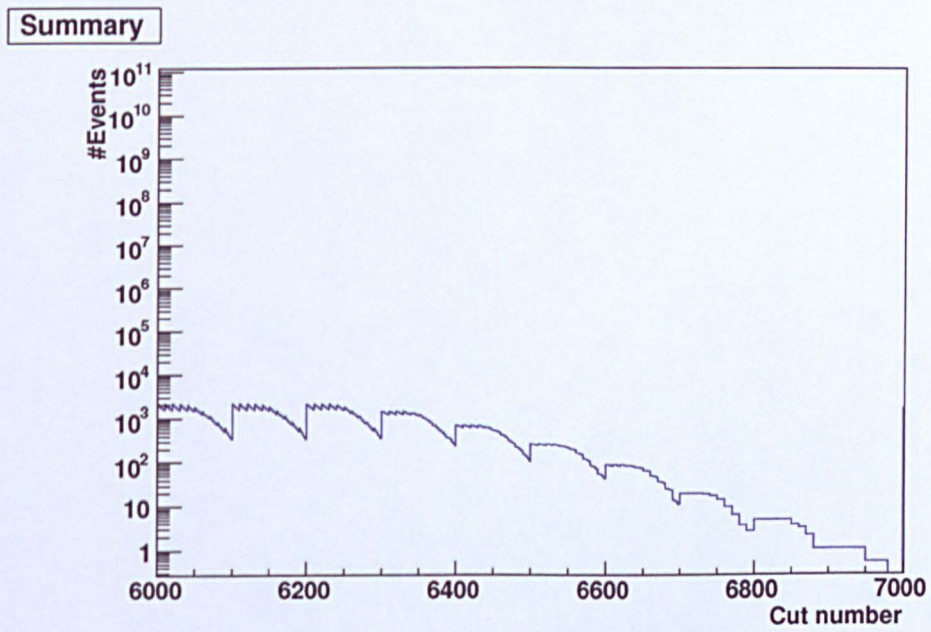

Figure 5.8: A zoom in of the plot in figure 5.7 on the left. The x axis is from 6000-7000.

Figure 5.8 shows part of the left plot in figure 5.7. A section of the x axis has been expanded to show some of the finer detail.

5.5.1 Significance

To find the optimum set of orthogonal cuts it is useful to define the significance.

$S = No.\ of\ Signal\ events\ that\ pass\ cuts$

$B = No.\ of\ Background\ events\ that\ pass\ cuts$

$$Significance = \frac{S}{\sqrt{S+B}}$$

This variable was used as it is a compromise between optimising for efficiency and optimising for purity. The plot in figure 5.9 shows the significance again with the abscissa on the x axis as discussed earlier.

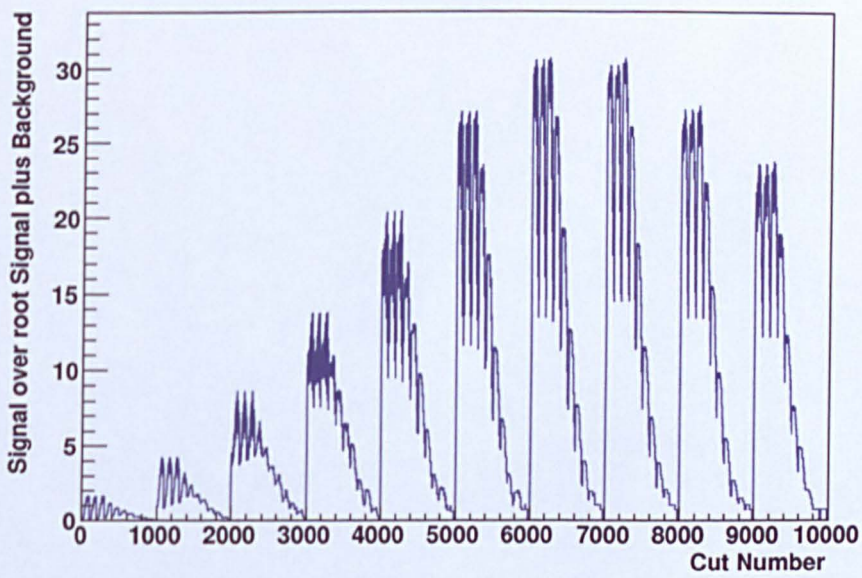

Figure 5.9: A plot showing how the significance varies as the cut values vary. The x axis is as described in the text

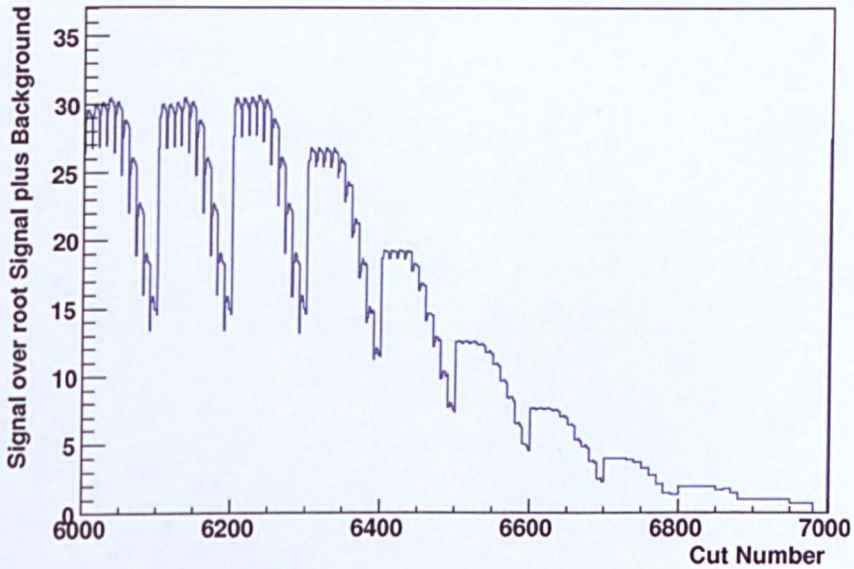

Figure 5.10: A zoom in of the plot in figure 5.9. The x axis shows from 6000-7000. The x axis is as described in the text.

Figure 5.10 shows a zoom in of part of the plot in figure 5.9 to show the finer detail. It is possible to see that the significance is dependent on the cut values, and by finding the highest point on this plot, the optimised set of cuts are found.

5.6 Sequential cuts

The cut values which resulted in the largest significance (the highest point on the figure 5.9 were (for the "SU3" point signal):

1. $E_T^{miss} > 300\ GeV$

2. 2 Jets or more $P_T > 50\ GeV$

3. P_T of Lead Jet $> 150\ GeV$

4. Sphericity > 0.04

Figure 5.11 show the 4 variables plotted with the optimised cuts applied sequentially.

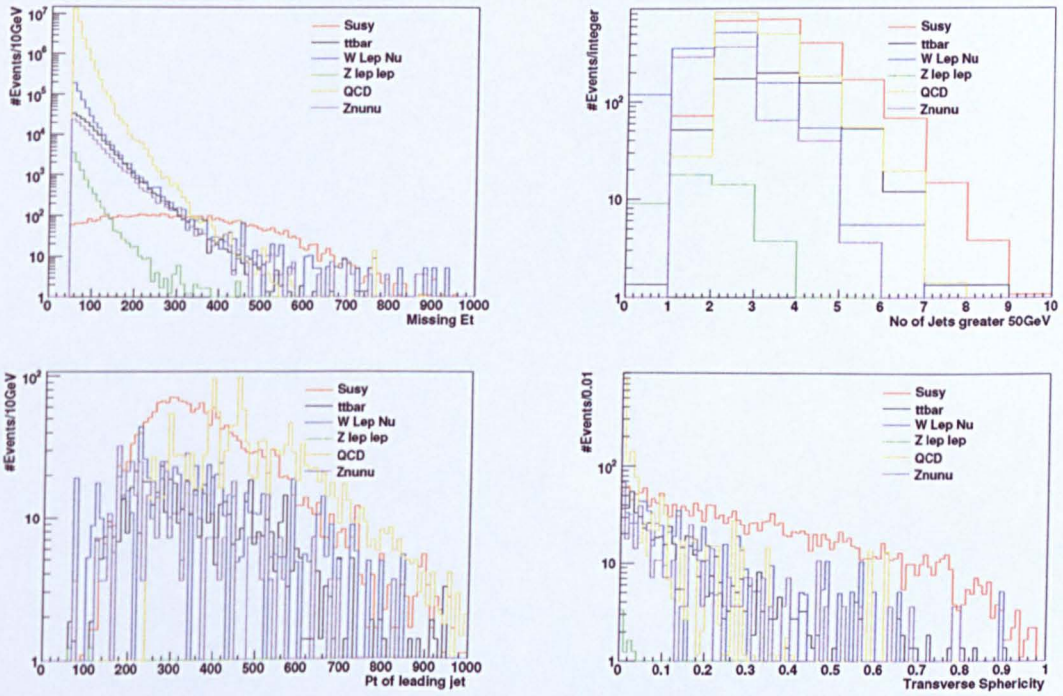

Figure 5.11: Plots that show sequential cuts as found in the cut optimisation for SU3. Top left only preselection cuts, top right after cut 1, bottom left cut after 1 and 2, bottom right after cut 1 to 3

Figure 5.11 may be used as a check that the optimisation procedure is performing correctly. The plot in the top left shows the E_T^{miss} distribution with only preselection cuts. The cut optimisation suggested a cut of $E_T^{miss} > 300\ GeV$, which seems sensible as a large portion of the backgrounds would be removed whilst the signal would be depleted to a lesser extent. The plot in

the top right shows the number of jets in each event with $P_T > 50\ GeV$. This plot is for for events where $E_T^{miss} > 300\ GeV$. The cut optimisation suggested removing events with less than 2 hadronic jets with $P_T > 50\ GeV$. Again this would remove a larger fraction of the background events than the signal so seems sensible. The plot in the bottom left is made for events with both $E_T^{miss} > 300\ GeV$, and with 2 hadronic jets or more with $P_T > 50\ GeV$. The optimisation procedure found that a cut requiring events to have a P_T of the lead jet of $> 150\ GeV$ was optimal. Whilst this removed more background events than signal it seems that the analysis is less dependent on this variable. Finally the sphericity was plotted (bottom right) with the optimised cuts on E_T^{miss}, the number of jets with $P_T. > 50\ GeV$, and P_T of the lead jet. A large spike from QCD events is removed by the optimised cut of 0.04, and less of the signal events.

The plots in figure 5.12 show how the effective mass varies as the optimised cuts were applied. The plot in the top left shows preselection cuts, top middle cut 1, top right cut 1-2, bottom left cut 1-3, bottom middle cut 1-4. The final plot in this figure shows how the significance varies by requiring events with cuts 1-4 and changing the required minimum effective mass.

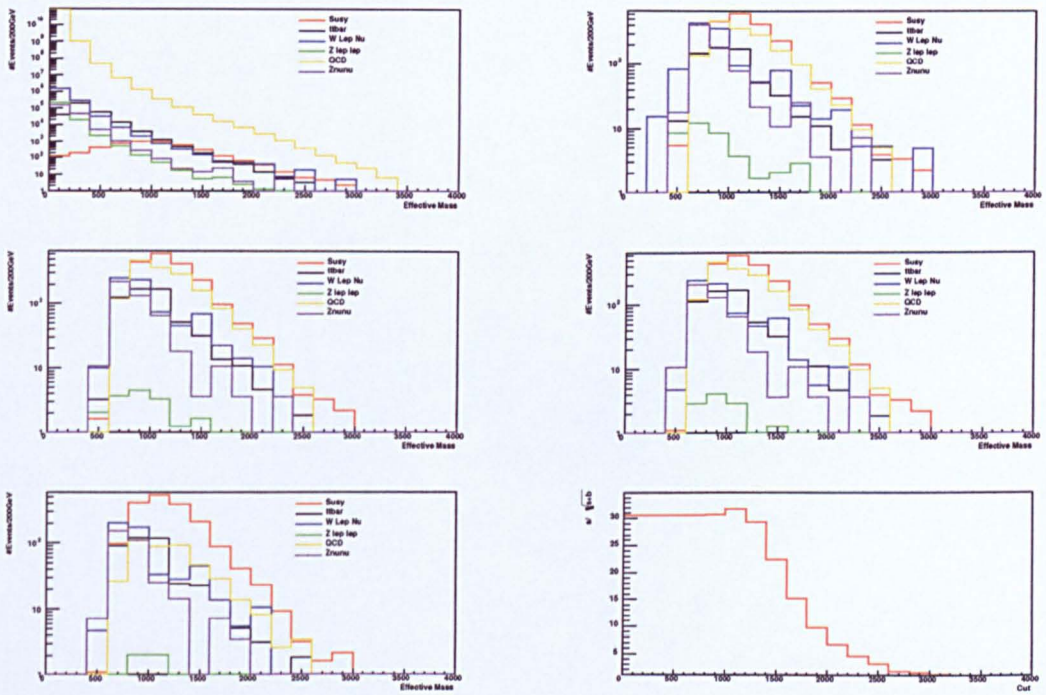

Figure 5.12: Plots showing how the effective mass varies with optimised sequential cuts. Top left no cuts, top right after cut 1, middle left after cut 1 and 2, middle right after cut 1 to 3, bottom left after cut 1 to 4, bottom right shows the significance as a function of cut on effective mass.

The above procedure was repeated for the different points in mSugra parameter space that were studied. The full set of results are shown in section 5.8.

5.7 Log likelihood based discrimination

Maximum likelihood estimation (MLE) is a statistical method which may be used to separate signal events from background events. In this case the model to be tested is a background only model. By using part of the background

samples, an expectation of what is 'background like' is formulated. The rest of the events are compared with this expectation and the Log Likelihood is a measure of the probability that an event is a background event.

5.7.1 Probability Density Functions

For a subset of the data, the background histograms were combined and then normalised to one to create probability density functions (PDF's) which are shown in figure 5.13. The same preselection cuts as the iterative method, of $E_T^{miss} > 50\ GeV$, and at least 1 hadronic jet were applied. A cut of zero leptons in the final state was also applied.

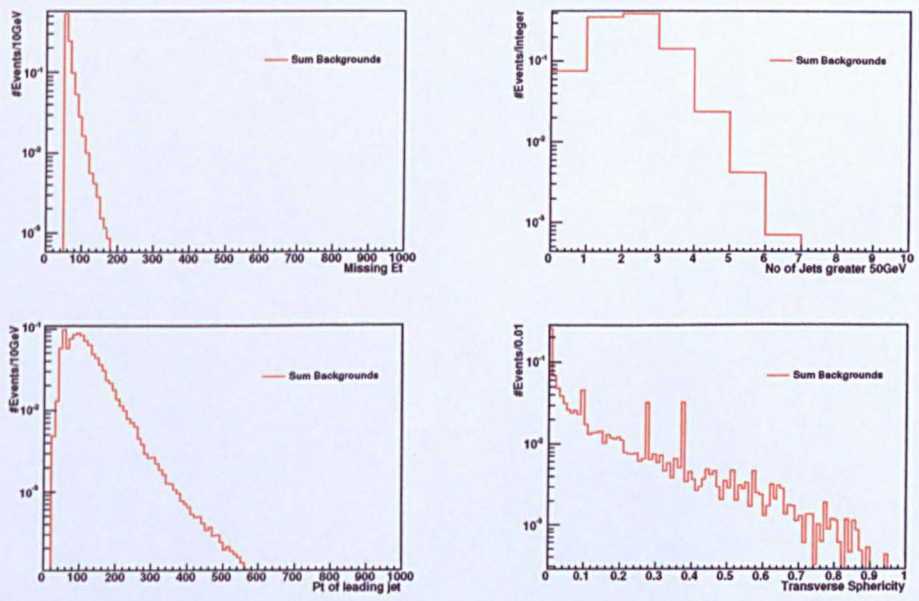

Figure 5.13: Plots showing the probability density functions for the backgrounds. The plots have missing energy (top left), number of jets with $P_T > 50\ GeV$ (top right), P_T of the lead jet (bottom left), and S_T (bottom right)

5.7.2 Log Likelihood background

Although the variables may not be strictly independent, they are going to be used in a log likelihood formulation as the resulting variable will be used as a discriminant. The remaining, statistically independent sample was treated as data. The probability of each variable having its value for each event was estimated using the PDFs, and the logs of these probabilities were added together. The logs of the probabilities were used rather than the probabilities themselves to prevent rounding errors on very small numbers. The resulting sum is the log likelihood. The distribution of this log likelihood is shown in figure 5.14 for signal (SU3 used as an example) and the background.

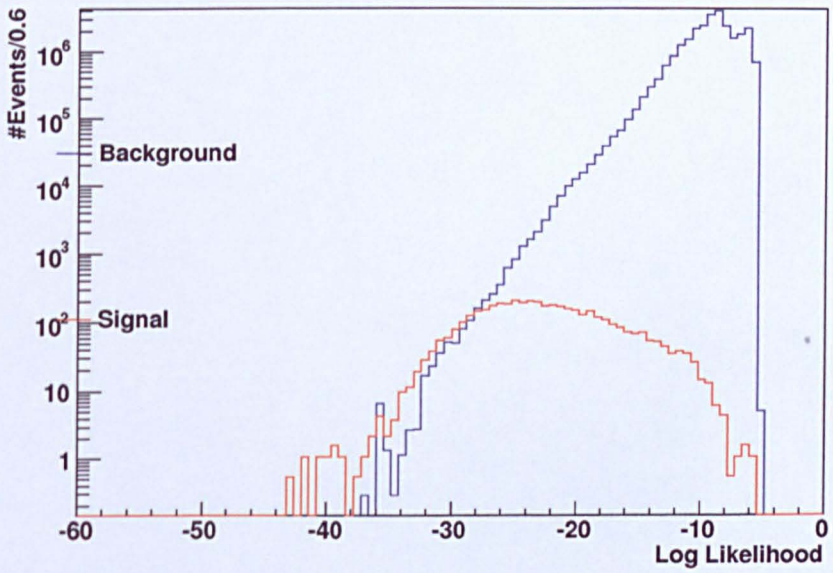

Figure 5.14: The log likelihood that each event is part of the background (for SU3 signal)

The more 'signal like' an event is, the more negative the value for the Log Likelihood becomes. By only accepting events with a log likelihood less than a given value, the significance may be optimised. The plot in figure 5.15 shows how the significance (see section 5.5.1) varies as a function of the bin (from the left to the right on the plot in figure 5.14) value to which the cumulative sum was performed.

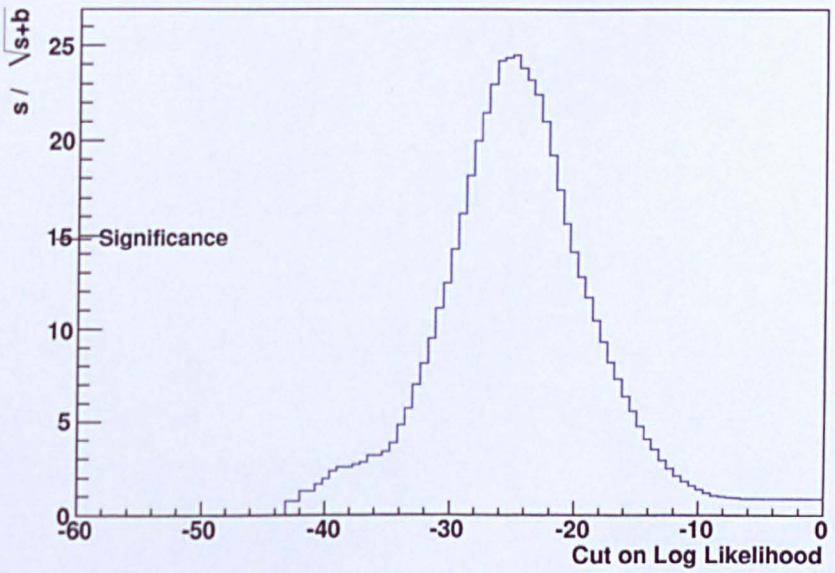

Figure 5.15: The significance as a function of cut(signal is again SU3)

This procedure for finding the Log Likelihood distribution and calculating the significance of a cut on this parameter was repeated for all of the mSugra points being studied. The results are presented in the next section.

5.8 Results and discussion

Table 5.7a shows the results from repeating the previous ATLAS analysis. The table shows the cuts made along with the significances obtained for each of the SUSY points studied. 5.7b shows the significances and the optimised cuts found by the iterative procedure for each point, and table 5.8 shows the significances for an optimised cut on the log likelihood parameter, again for each point. The efficiencies are also shown in these tables, and whilst they do not take account of trigger efficiencies, the events should pass either the jet triggers or the E_T^{miss} triggers (see chapter 2) with high efficiency.

It may be seen from these tables that optimising the cuts for each SUSY point increases the resulting significance and will distinguish signal from background for a lower integrated luminosity. Whilst the log likelihood method of optimising does perform better than the standard ATLAS cuts, it does not outperform the optimal cuts based analysis. It should be noted that the log likelihood method is computationally faster and more readily extensible to include new variables than the method of looping over all possible combinations of cut values. The Log Likelihood method is not superior to the optimised orthogonal cuts as the variables are not fully independent of each other and it was thought that the log likelihood technique was more sensitive to this than the optimised cuts method.

Label	Previous Atlas analysis	Significance	Signal Efficiency	Background Efficiency
SU1	At least four jets with P_T > 50 GeV one of which must have P_T > 100 GeV; and MET > 100 GeV	5.3	0.13	2.6×10^{-10}
SU3	MET > 0.2 Effective mass	12.0	0.14	2.6×10^{-10}
SU4	Transverse Sphericity >0.2	68.3	0.06	2.6×10^{-10}
SU6	$\Delta\phi(jet_1 - MET) > 0.2, \Delta\phi(jet_2 - MET) > 0.2, \Delta\phi(jet_3 - MET) > 0.2$	3.4	0.16	2.6×10^{-10}
SU8.1	Reject event with an e or a with P_T greater than 10 GeV	4.6	0.15	2.6×10^{-10}
	Effective Mass >800 GeV			

Label	E_T^{miss} > (GeV)	#Jets with P_T > 50GeV	P_T of Lead Jet > (GeV)	S_T >	Significance	Signal Efficiency	Background Efficiency
SU1	350	2	150	0.06	19.2	0.28	4.5×10^{-11}
SU3	300	2	150	0.04	30.7	0.33	1.3×10^{-10}
SU4	150	2	50	0.07	97.2	0.26	4.5×10^{-9}
SU6	450	2	150	0.03	12.8	0.22	1.5×10^{-11}
SU8.1	350	2	150	0.06	17.0	0.32	4.5×10^{-11}

Table 5.7: Tables showing the significances and efficiencies for each mSugra point for standard cuts and for optimised orthogonal cuts Table 5.7a (left) shows the cuts from the earlier ATLAS study, and the significances obtained. Table 5.7b (right) shows the optimised cuts as found by the iterative procedure and the significance obtained.

Label	Optimal Log Likelihood Cut Value	Significance	Signal Efficiency	Background Efficiency
SU1	-28.5	15.7	0.30	1.09×10^{-10}
SU3	-26.7	24.5	0.30	2.3×10^{-10}
SU4	-20.8	79.5	0.28	8.8×10^{-9}
SU6	-29.7	11.3.	0.27	4.4×10^{-11}
SU8.1	-29.1	14.1	0.35	1.1×10^{-10}

Table 5.8: A table showing the significances and efficiencies as calculated for the optimal log likelihood cut for each mSugra point

5.9 Treatment of Systematic Uncertainties

Introduction

Systematic errors are biases in a measurement that result in the mean of a large number of measurements differing significantly from the actual value. There are 4 main sources of systematic errors that will affect this study. They are:

- Imprecise knowledge of the luminosity
- Predicted cross sections being incorrect
- Problems with the jet energy scale
- E_T^{miss} not being calibrated

If the inital luminosity of the colliding protons is not known exactly, then all of the distributions will be scaled up or down. More or less events, both signal and background, will pass cuts. In a counting experiment this will cause problems as it may indicate discovery or exclusion incorrectly.

If one or all of the cross sections are incorrect, this will cause similar problems to imprecise knowledge of the luminosity. In the case of the LO generators, the cross sections are only calculated to first order. With NLO generators, the feynman diagrams from the next order are also used. This means that the generators are only approximating the cross-sections, not caluculating them absolutely, and to varying degrees or precision.

The momentum of the interacting partons is not know exactly either. Rather it has been measured at low energies and the effect of increasing energy is calculated. The effect of not knowing the PDFs exactly will have an effect on the calcuated cross section [42].

The jet energy scale [39] is the conversion of calorimeter energy to parton energy. After the partons hadronise and shower in the calorimeter, the cone algorithm [27] is used to reconstruct the energy. There are however various corrections to this energy, such as underlying event corrections, final state radiation corrections starting from the hard collision, and 'out-of-cone' corrections, where part of the jet energy is not reconstrcted. Known SM processes will be used to determine the jet energy scale [39, 27]. Three ranges of P_T are used to summarise this effect. These are:

- for 10 GeV to $100 - 200$ GeV the effect is $5 - 10\%$
- $100 - 200$ GeV to 500 GeV the effect is $1 - 2\%$
- Above 500 GeV a few per cent.

E_T^{miss} has a large amount of discriminating power in the search for mSugra Supersymmetry. It is however a complicated variable and will need to be calibrated. A method for doing this with data is discussed in chapter 4.

Scaling the backgrounds

By artificially varying the cross section for each of the backgrounds, it is possible to consider the case of the cross sections for the backgrounds being incorrect, and calculate errors for the iterative cuts based analysis. The individual backgrounds were scaled up and down by 20% and the analysis repeated. 20% was chosen to be greater than the effect the jet energy scale may have, and to allow for a small deviation in cross section and other effects. New sets of optimised cuts were found and the resulting significances re-calculated. Tables 5.9 - 5.13 show the resulting errors.

Background	Variation	$Significances \pm error$
ttbar	20%	19.2 ± 0.19
QCD	20%	19.2 ± 0.17
$W \rightarrow l\nu$	20%	19.2 ± 0.33
$Z \rightarrow l^+l^-$	20%	19.2 ± 0.01
$Z \rightarrow \nu\nu$	20%	19.2 ± 0.19

Table 5.9: Systematic errors for SU1 for varying backgrounds

Background	Variation	$Significances \pm error$
ttbar	20%	30.7 ± 0.18
QCD	20%	30.7 ± 0.24
$W \rightarrow l\nu$	20%	30.7 ± 0.17
$Z \rightarrow l^+l^-$	20%	30.7 ± 0.00
$Z \rightarrow \nu\nu$	20%	30.7 ± 0.11

Table 5.10: Systematic errors for SU3 for varying backgrounds

Background	Variation	*Significances ± error*
ttbar	20%	97.2 ± 1.18
QCD	20%	97.2 ± 4.20
$W \rightarrow l\nu$	20%	97.2 ± 0.78
$Z \rightarrow l^+l^-$	20%	97.2 ± 0.01
$Z \rightarrow \nu\nu$	20%	97.2 ± 0.42

Table 5.11: Systematic errors for SU4 for varying backgrounds

Background	Variation	*Significances ± error*
ttbar	20%	12.8 ± 0.10
QCD	20%	12.8 ± 0.10
$W \rightarrow l\nu$	20%	12.8 ± 0.26
$Z \rightarrow l^+l^-$	20%	12.8 ± 0.01
$Z \rightarrow \nu\nu$	20%	12.8 ± 0.10

Table 5.12: Systematic errors for SU6 for varying backgrounds

Background	Variation	*Significances ± error*
ttbar	20%	17.0 ± 0.19
QCD	20%	17.0 ± 0.16
$W \rightarrow l\nu$	20%	17.0 ± 0.31
$Z \rightarrow l^+l^-$	20%	17.0 ± 0.01
$Z \rightarrow \nu\nu$	20%	17.0 ± 0.18

Table 5.13: Systematic errors for SU8.1 for varying backgrounds

For all of the points the $Z \rightarrow l + l$ background had the least systematic effect, with the QCD, ttbar, and $W \rightarrow l + \nu$ having more impact. If the variation in background is 100% correlated the largest effect is a 6.8% change for the SU4 sample and the smallest is 2.2% for SU3.

5.10 Summary

The Signal and background samples were introduced and discussed. A previous ATLAS analysis [27] was repeated and the significances calculated. This was compared for each point to an optimised selection procedure. Next a log likelihood was computed for each point, and used as a parameter to preferentially select signal. Finally systematic errors were considered and presented. It is worth noting that whilst the systematic of incorrect background cross section was investigated there are other sources of systematics. The detector will have to be extensively calibrated to achieve the significances shown in this study.

The next chapter looks at how much data needs to be collected before these points can be excluded, or discovered.

Chapter 6

Confidence Levels

In order to correctly interpret the results produced in the SUSY analysis, a framework must be introduced. This will enable predictions to be made as to how much data is needed before either discovering or excluding a particular SUSY point.

6.1 Confidence Levels

Confidence levels (CL_x) are used to measure the degree of compatibility the results have with an hypothesis x.

The confidence level for a background only hypothesis is defined as:

$$CL_b = P_b\left(X \leq X_{obs}\right) = \int_0^{X_{obs}} \frac{dP_b}{dX} dX$$

where X is the test statistic used to separate non-background like data from background like data, and $\frac{dP_b}{dX}$ is the Probability Distribution Function (PDF) of X. The integration of $\frac{dP_b}{dX}$ up to the observed value of X, (X_{obs})

gives the confidence level for the background only hypothesis.

As the presence of a signal is in addition to the known background rate, we can also test for compatibility of the data with a signal + background hypothesis. The confidence level in the signal + background hypothesis, CL_{s+b} in a similar way is:

$$CL_{s+b} = P_{s+b}(X \leq X_{obs}) = \int_0^{Xobs} \frac{dP_{s+b}}{dX} dX$$

X is again the test statistic, and $\frac{dP_{s+b}}{dX}$ is the PDF whose integration up to a certain value of X_{obs} yields the confidence level. There is however a problem with using CL_{s+b} as it assumes a perfect background model. It is possible that no signal combined with an overestimated background could lead to an artificially inflated exclusion limit. To circumvent this the Modified Frequentist (MF) [43] approach can be taken, and it is useful to introduce CL_s as:

$$CL_s \equiv \frac{CL_{s+b}}{CL_b}$$

In this case the confidence level for *signal + background* is normalised to the confidence level for *background*. CL_s is actually a ratio of confidence levels rather than a true confidence level.

With a signal test, the value of $1-CL_b$ may be used to distinguish between a null and a signal hypothesis. It is usual for a discovery to be announced when a 5σ deviation between data and the expected backgrounds is found. The value of $1 - CL_b$ may be used to measure the degree of significance of an excess. In the same way that CL_s was normalised to the background

distribution, it is prudent to use the following:

$$\frac{1 - CL_b}{1 - CL_{s+b}}$$

where $1 - CL_b$ is normalised to the *signal + background* distribution. A comparison of the confidence level definitions is given in the next section.

6.2 Comparison of Confidence Level Definitions

Examples are presented to illustrate how the confidence levels defined in the previous section apply to a simple counting experiment. Just the number of expected background and expected signal candidates are used as input, and CL_s and CL_{s+b} are shown in the context of exclusion and discovery calculations.

Firstly, we investigate the case of a low signal rate compared to the total background. Figure 6.1 shows an example with 40 background events, and 5 signal events. The top half of the figure shows the PDFs which are Poisson distributions of the expected number of events for the two hypotheses. One Poisson is for the background only case, and one is for signal + background. If the number of events actually observed in the experiment (N_{obs}) falls in the middle of the two distributions it is clear that is hard to tell which hypothesis is correct.

The lower half of figure 6.1 shows how CL_s and CL_{s+b} evolve with increasing N_{obs}. The dashed line indicates the point at which CL_s and CL_{s+b} fall below 0.05, which is analogous to an exclusion of the signal to 95% CL.

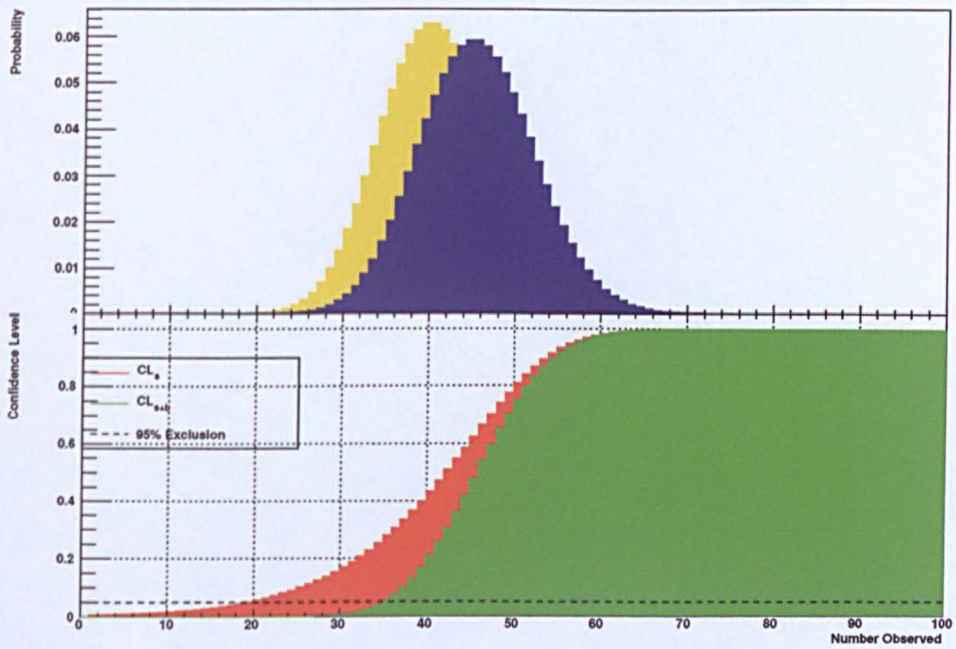

Figure 6.1: Confidence Level example for a low signal rate with the Poisson distributions shown in the top half for a background only expectation of 40 and background + signal of 45. The bottom half shows the corresponding values of CL_s and CL_{s+b} as a function of number observed.

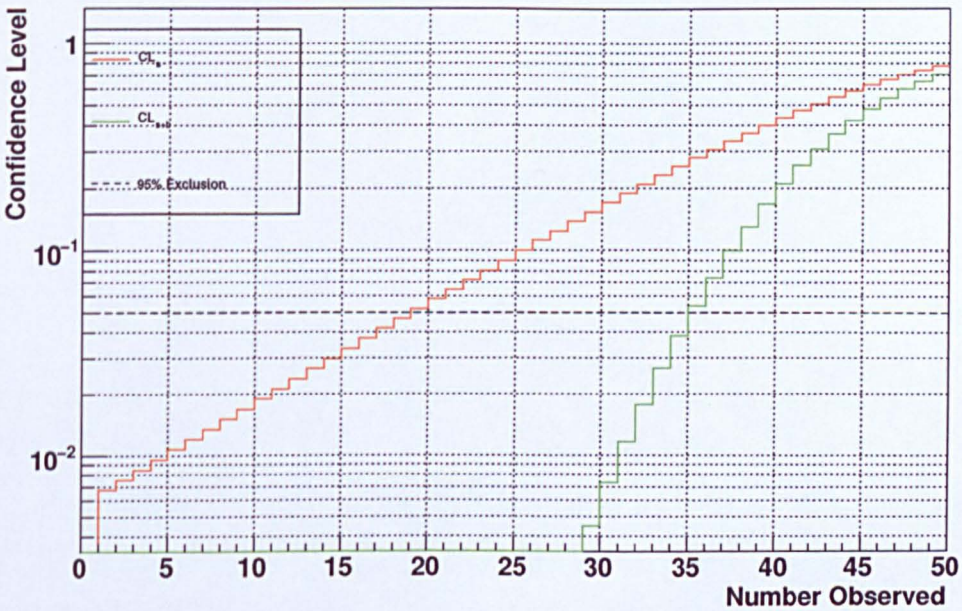

Figure 6.2: Confidence Level example at low N_{obs} for closely space distributions. CL_s and CL_{s+b} are shown relative to the 95% CL exclusion limit, which is the dashed line.

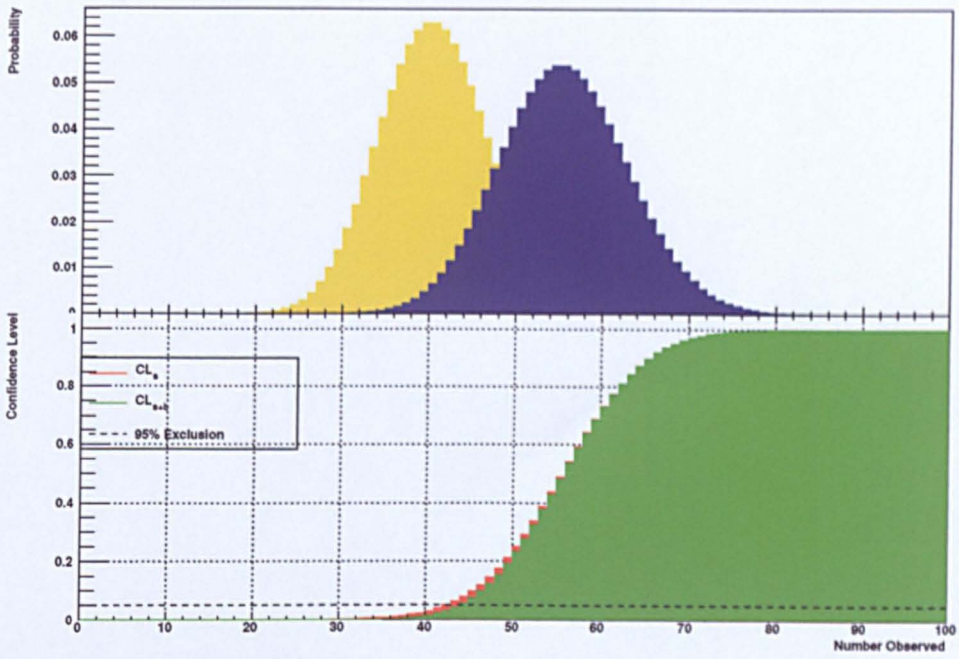

Figure 6.3: Confidence Level example for a high signal rate with the Poisson distributions shown in the top half for a background only expectation of 40 and *background + signal* of 60. The bottom half shows the corresponding values of CL_s and CL_{s+b} as a function of number of events observed experimentally.

Figure 6.2 shows the points at which CL_s and CL_{s+b} fall below the 0.05 line in more detail. It may be seen that using CL_{s+b} , the signal would be excluded by observing less than 35 events, whereas with the CL_s method less than 20 events must be observed before the signal can be excluded. The CL_s method is therefore more conservative.

The second example (shown in figure 6.3) examines the case where there is a good separation of the background only and the signal + background distributions. The bottom half of figure 6.3 shows that with a good separation in these PDFs the different confidence level definitions, CL_s and CL_{s+b}, tend

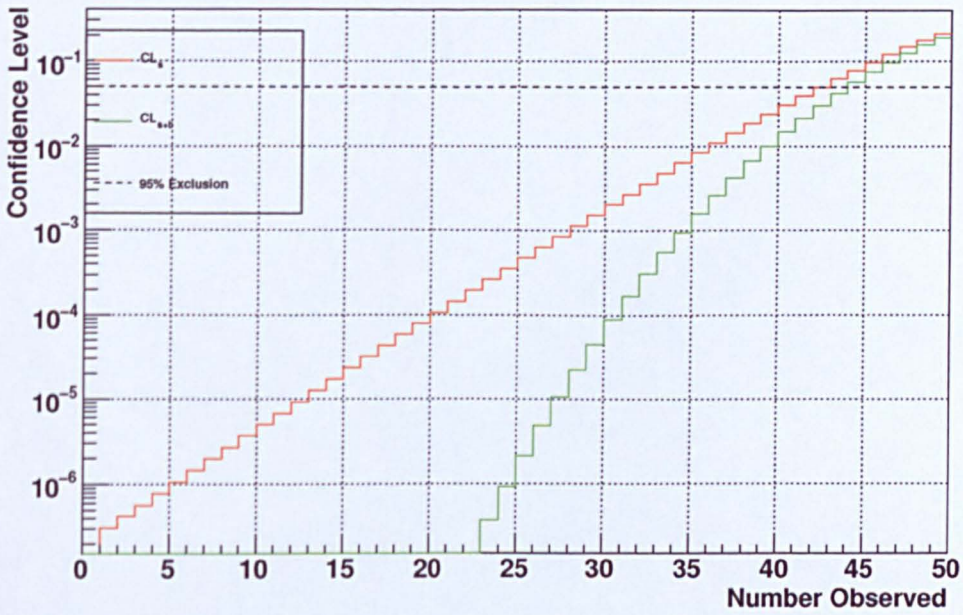

Figure 6.4: Confidence Level example at low N_{obs} for well spaced distributions. CL_s and CL_s are shown relative to the 95% CL exclusion limit, which is the dashed line.

to converge.

Figure 6.4 shows in more detail the evolution of CL_s and CL_{s+b} as they cross 0.05, the point at which the signal may be excluded to 95% confidence level. It may be seen that for the well separated example the value of N_{obs} needed for exclusion differs by only one event.

As discussed in the previous section, and analogous to the CL_s method, figure 6.5 shows a discovery example for a low signal rate. The PDF distributions are shown in the top half, and the evolution of $1 - CL_b$ and $\frac{1-CL_b}{1-CL_{s+b}}$ are shown in the bottom half.

Figure 6.6 shows in more detail the points at which these curves cross the 3σ and 5σ boundaries. It is on crossing the 5σ boundary that a discovery

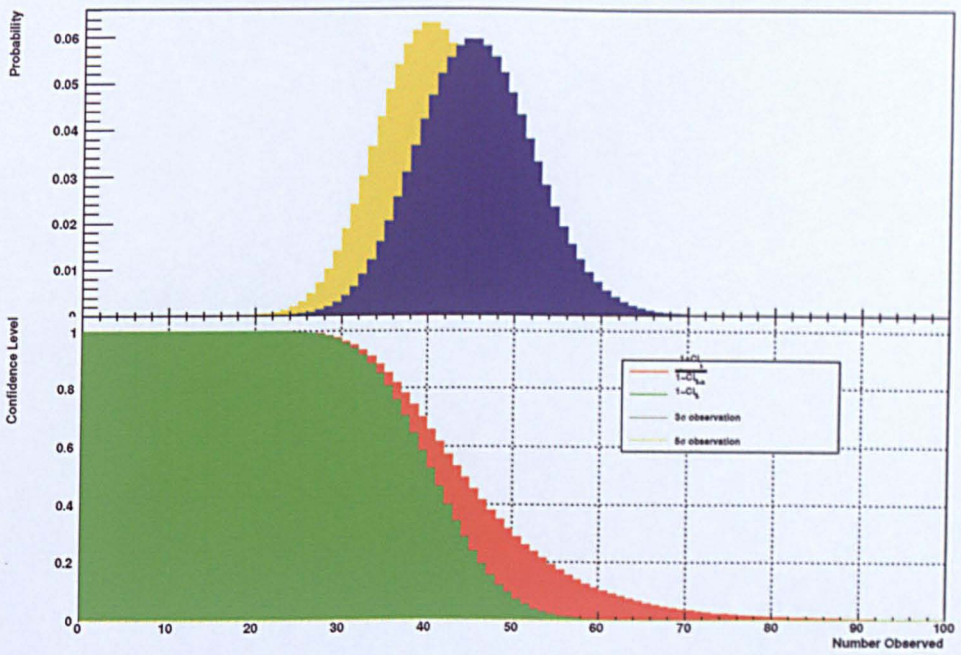

Figure 6.5: Discovery potential example with the Poisson distributions shown in the top half for a background only expectation of 40 and background + signal of 45. The bottom half shows the corresponding values of $1 - CL_b$ and $\frac{1-CL_b}{1-CL_{s+b}}$ as a function of number observed.

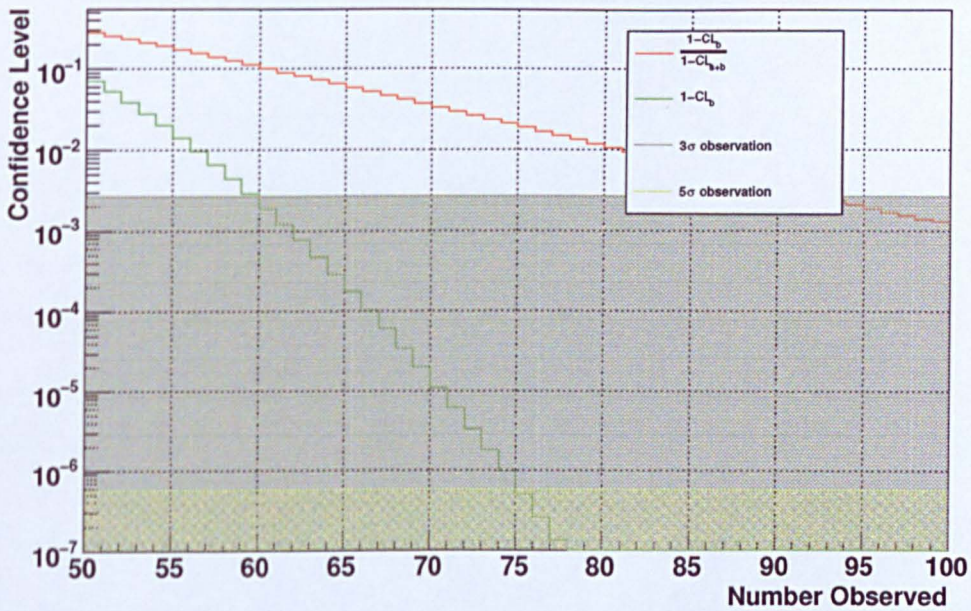

Figure 6.6: Discovery potential at high N_{obs} for closely spaced distributions. $1-CL_b$ and $\frac{1-CL_b}{1-CL_{s+b}}$ are shown relative to the 3σ and 5σ discovery boundaries.

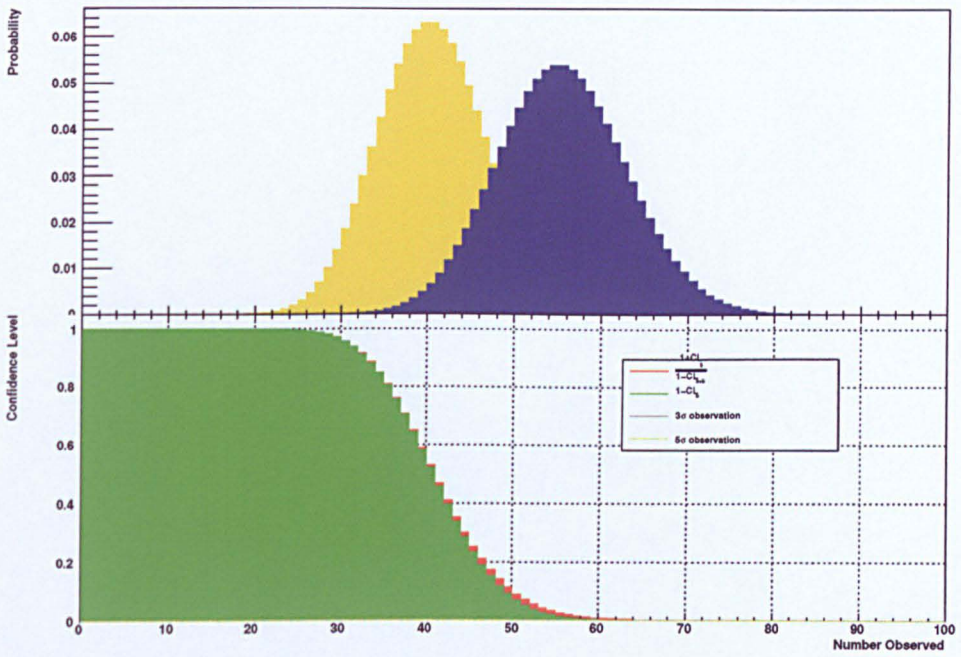

Figure 6.7: Discovery potential example with the Poisson distributions shown in the top half for a background only expectation of 40 and background + signal of 55. The bottom half shows the corresponding values of $1-CL_b$ and $\frac{1-CL_b}{1-CL_{s+b}}$ as a function of number observed number of events.

is conventionally announced. It can be seen that $(1 - CL_b)$ announces a discovery for a value of N_{obs} of 75, whereas using the $\frac{1-CL_b}{1-CL_{s+b}}$ method far more than 100 events are needed.

Looking at a high signal rate, figure 6.7 shows the Poisson distributions and the evolution of $1 - CL_b$ and $\frac{1-CL_b}{1-CL_{s+b}}$. It can be seen that as the distributions separate the values for these two methods converge once again.

Figure 6.8 show that for a 5σ discovery, the difference in these two methods is now roughly 15 events.

The main observation from these examples should be that normalising the confidence level to the background in the case of CL_s, and to the

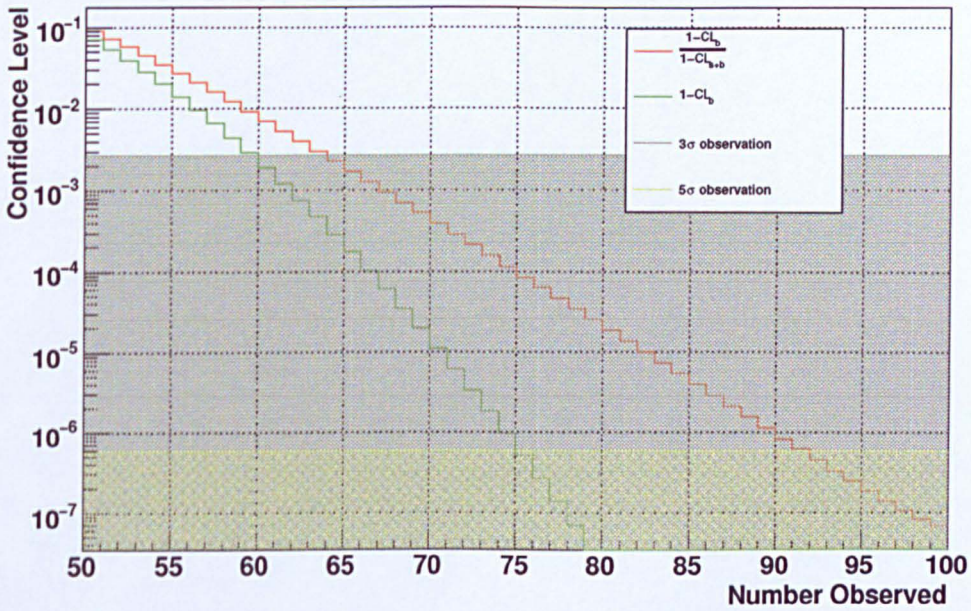

Figure 6.8: Discovery potential at high N_{obs} for well separated distributions. $1 - CL_b$ and $\frac{1-CL_b}{1-CL_{s+b}}$ are shown relative to the 3σ and 5σ discovery lines.

signal + background in the case of $\frac{1-CL_b}{1-CL_{s+b}}$ gives a test of a hypothesis that is conservative in both discovery and exclusion. These variables will be put to more use in the next section.

6.3 SUSY prospects

The SUSY analysis presented in chapter 5 predicts (for a given luminosity) the number of events that will pass the selection for background only, and also for signal + background for an average experiment. This is to say that if the experiment was repeated a large number of times, one would expect N_{obs} to follow a Poisson distribution with a mean equal to the MC prediction.

As the luminosity collected by an experiment increases, the mean number of expected events will scale. As the amount of data increases, the means of the background only and the signal + background distributions will separate. The more data taken, the easier it is to tell signal from background.

The final part of this chapter will interpret these results and answers the question:

"Once the detector is perfectly calibrated, how much luminosity is needed to exclude the mSugra points studied, and for each point how much data would be needed to make a discovery if nature had chosen this model?"

6.3.1 Exclusion

By varying the Poisson distributions to account for a range of luminosities, it is possible to estimate at what luminosity an observed value N_{obs} equal to the predicted background excludes the existence of the signal to $95\%CL$.

mSugra Point	Luminosity needed to exclude to $95\%CL$
SU1	$12pb^{-1}$
SU3	$5pb^{-1}$
SU4	$\sim 1pb^{-1}$
SU6	$25pb^{-1}$
SU8	$15pb^{-1}$

Table 6.1: The luminosity at which the mSugra points can be excluded to $95\%CL$

This is simulating the most probable background only experiment.

Figure 6.9 shows CL_s as luminosity increases for each of the mSugra points. It should be clear that all of the points may be excluded with less than $30pb^{-1}$.

Table 6.1 shows for each mSugra point, the luminosity at which CL_s crosses the $95\%CL$ line.

6.3.2 Discovery

Again the Poisson distributions were varied to match different luminosities, but this time N_{obs} was set to be equal to the *signal + background* prediction for each luminosity. This simulates the most probable experiment in which the signal is present.

Figure 6.10 shows the discovery potential as a function of increasing luminosity. The 3σ and 5σ boundaries are shown. It should be immediately clear that all of the points can be discovered to 5σ with less than $60pb^{-1}$.

Table 6.2 shows the necessary luminosity to obtain a $3\sigma$and a 5σ discovery for each SUSY point investigated.

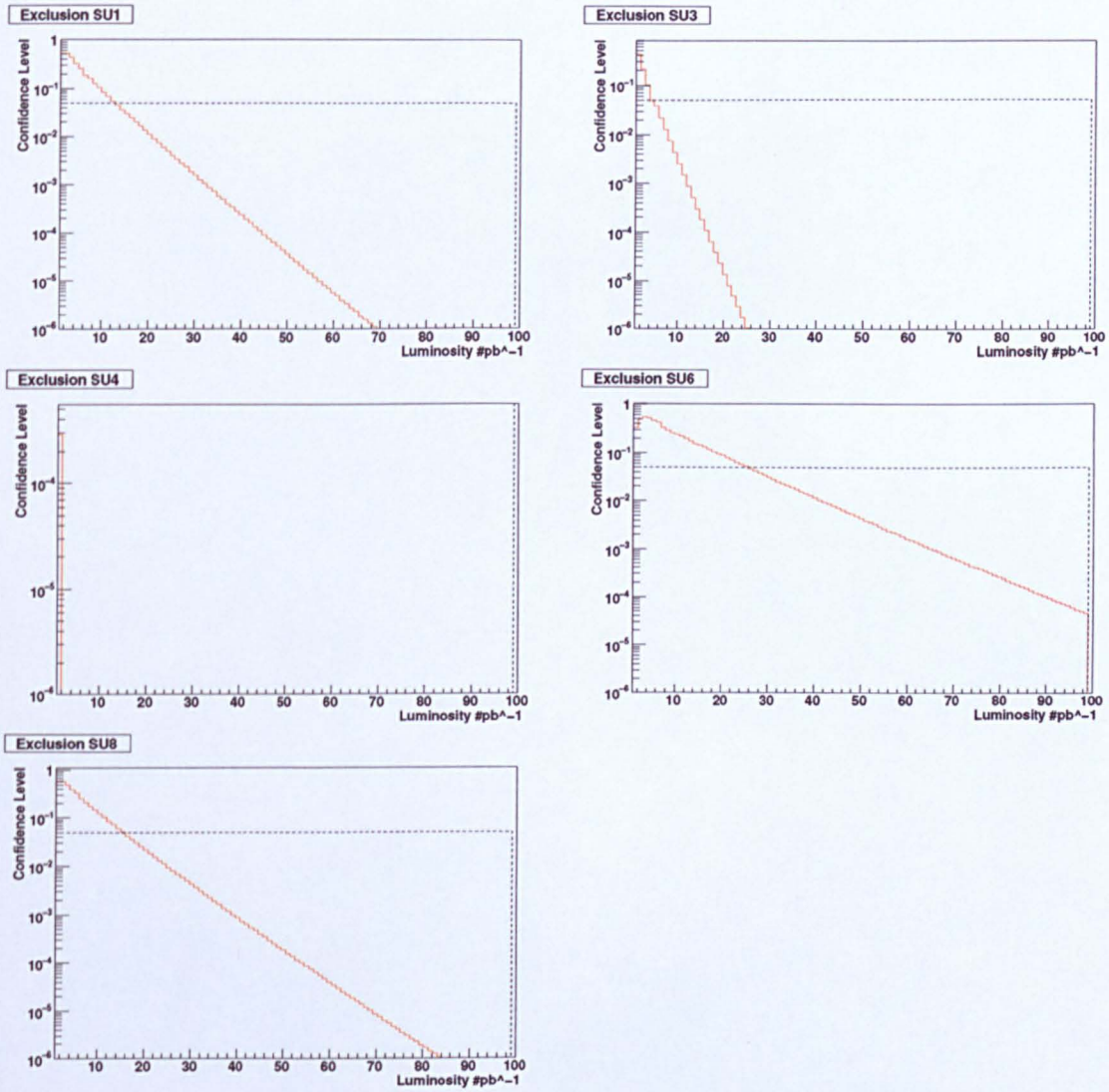

Figure 6.9: For the SUSY points studied, $CL_s \equiv \frac{CL_{s+b}}{CL_b}$ as a function of luminosity with CL_{s+b} and CL_b (this is 0.5) integrated up to expected background. Also shown is the 95% exclusion line.

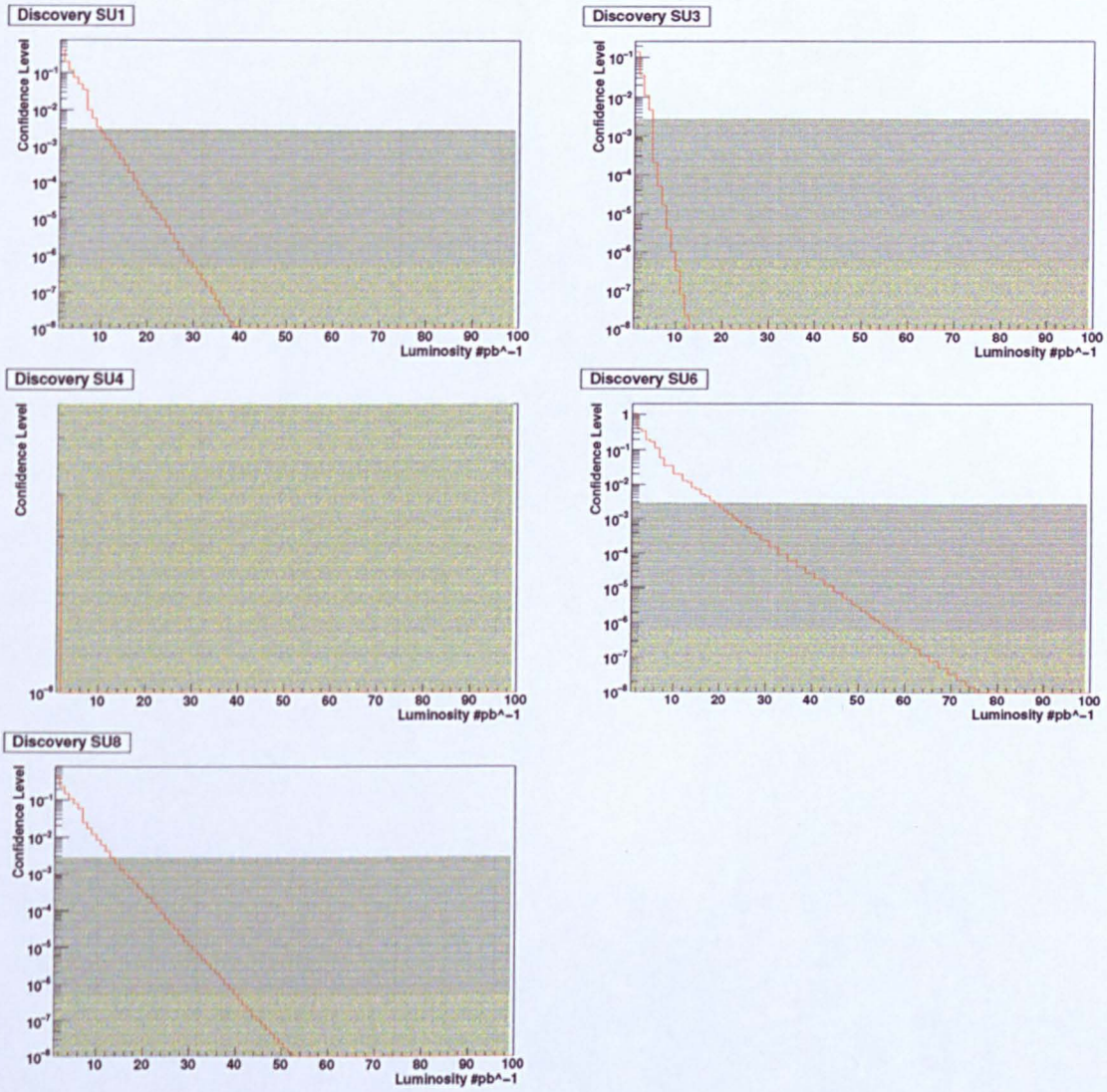

Figure 6.10: For the SUSY points studied, $\frac{1-CL_b}{1-CL_{s+b}}$ as a function of luminosity with $1-CL_b$ and $1-CL_{s+b}$integrated up to expected $signal+background$. Also shown are the 3σ and 5σ discovery bounds.

mSugra Point	Luminosity needed observe to 3σ	Luminosity needed to discover to 5σ
SU1	$10pb^{-1}$	$30pb^{-1}$
SU3	$5pb^{-1}$	$10pb^{-1}$
SU4	less than $1pb^{-1}$	less than $1pb^{-1}$
SU6	$20pb^{-1}$	$57pb^{-1}$
SU8	$14pb^{-1}$	$40pb^{-1}$

Table 6.2: The luminosity at which the mSugra points could be discovered to 3σ and 5σ

6.4 Summary

In this chapter Confidence Levels were introduced and examples demonstrated that the Modified Frequentist method is conservative in both discovery and exclusion. The ideas of Confidence Levels were applied to the analysis presented in chapter 5, and by taking the case of the most likely experiment, we estimate how much data must be accumulated before a point is excluded or discovered.

Whilst this treatment only includes statistical errors and not systematic errors, it is possible to consider the case of a well calibrated detector. It was found that less than $30pb^{-1}$is needed to exclude all of the points in the absence of signal, and less than $60pb^{-1}$ of data is needed to discover these points.

As it is expected that ATLAS will produce $200pb^{-1}$ in its first year of running, it is clear that a good early understanding of the detector (and thus the systematics) is vital. If SUSY is found, the next job will be to determine which model is correct.

Chapter 7

Conclusions

The full discovery potential of the ATLAS experiment at the LHC will require the commissioning and calibration of the apparatus. This will be an ongoing effort to constantly gain a better understanding of the detector performance. However some of the signals predicted for beyond the SM scenarios should be accessible at an early stage even with non optimal calibrations. For example one of the key variables used in this analysis is E_T^{miss} and the study described in chapter 4 shows how the resolution of this quantity may be found from data and compared to simulations. The predicted signals from SUSY are much larger than the predicted resolutions and should not be very sensitive if the resolution is larger than predicted by simulation. In any case the actual resolution will be measured using data.

Although the mechanism for the breaking of SUSY (see chapter 1) is not known many models predict that the variables used in this analysis (see chapter 5) will help to distinguish SUSY events from background processes. The mSugra simulations used are examples of topologies expected. Two

techniques were studied to optimise the selection of SUSY events.

The cut based analyses show that the optimisation depends on the particular mSugra point and relies heavily on the large values of missing transverse energy to separate the signal from the backgrounds. Also important for the discrination of signal from background are the other variables considered: the P_T of the lead jet; the number of jets with P_T greater than 50 GeV; the transverse sphericity. The analysis depends on knowing the levels of the backgrounds but varying the cross sections by 20% still allows a good signal to background ratio with the cuts used.

The log likelihood analysis was applied to the same data and very similar results were obtained. One advantage of this analysis technique is that it searches for a deviation from the SM background, and as such we are searching for excesses and not comparing to a signal. The examples shown are for the mSugra points described but the technique is sensitive to any new physics for which the variables used offer some discrimination against background.

The study of confidence levels indicates that the presence or absence of SUSY should become apparent very quickly once the LHC begins to deliver colliding beams. This study has assumed that the initial collision energy will be 10 TeV. It is now known that due to the delay in the LHC start up the initial collision energy will be 7 TeV which will be gradually increased. Nevertheless the general conclusion is that it should be possible to claim either the discovery of SUSY or place upper limits on some of the existing models with the early data.

Bibliography

[1] B.R. Martin and G. Shaw, *Particle Physics.* John Wiley and Sons, second ed., 1997

[2] F. Halzen and A. Martin, *Quarks and Leptons;* An Introductory Course in Modern Particle Physics. John Wiley and Sons, 1984

[3] L.H. Ryder, *Quantum Field Theory.* Cambridge University Press, second ed., 1996

[4] I.J.R. Aitchison and A.J.G. Hey, *Gauge Theories in Particle Physics,* IOP Publishing Ltd., Bristol 1989

[5] P.Renton, *Electroweak Interactions,* Cambridge University press, Cambridge, 1990.

[6] D.Perkins, *Introduction to High Energy Physics,* Addison-Wesley, 1987

[7] BackReAction http://backreaction.blogspot.com/2007_12_01_archive.html

[8] *Proceedings of the School for Experimental High Energy Physicsts Students held 3 to 15 September 2006,* June 2007

[9] S.L. Glashow, Nucl. Phys. 22, 579 (1961)

[10] A. Salam and J.C Ward, *Phys. Lett.* 13, 168 (1964)

[11] S.Weinberg *Phys. Rev. Lett.* 19, 1264 (1967)

[12] G. 't Hooft et al, *Recent Developments in Gauge Theories*, Plenum Press, New York, 1980

[13] C. Lee, B. Quigg and H.Thacker, *Phys. Rev.* D16, 1519 (1977)

[14] The LEP Collaborations, *A Combination of Preliminary Electroweak Measurements and constraints on the Standard Model.* arXiv:hep-ex/0511027v2, 2005

[15] ALEPH, DELPHI, L3 and OPAL collaborations, *Search for the Standard Model Higgs Boson at LEP, Phys. Lett.* B565 (2003) 61

[16] The Tevatron New-Phenomena and Higgs Working Group, *Combined CDF and D0 Upper Limits on Standard Model Higgs Boson Production at High Mass (155-200 GeV/c^2) with 3 fb^{-1} of data.* arXiv:hep-ex/0808.0534v1, 2008

[17] S.P. Martin, *A Supersymmetry Primer.*arXiv:hep-ph/9709356v5, 1997.

[18] J.Wess and B.Zumino, *A Lagrangian Model Invariant Under supergauge Transformations*, Phys. Lett B49 (1974) 52.

[19] S.P. Martin, *Perspectives on Supersymmetry*, World Scientific, Singapore, 1998

[20] G.Farrah and P. Fayet Phys. *Lett.* B76, 575 (1978)

[21] L. Randall and R. Sundrum, *Out Of This World Supersymmetry Breaking,* Nucl. Phys. B557 (1999) 79-118

[22] Higgs mechanism Wikipedia http://en.wikipedia.org/wiki/Higgs_mechanism

[23] Hybids of Art and Science http://hybridsofartandscience.blogspot.com/

[24] The ATLAS Fact Sheet, http:///atlas.ch

[25] Parton Distribution Functions http://www.finestructure.com/2008/09/parton-distribution-functions/

[26] The ATLAS Collaboration, G. Aad et al., The ATLAS Experiment at the CERN Large Hadron Collider, JINST 3 (2008) S08003.

[27] The ATLAS Collaboration, *Expected performance of the ATLAS Experiment, Detector, Trigger and Physics.* CERN-OPEN-2008-020, Geneva, 2008

[28] G. Corcella et.al., "Herwig 6.5: an event generator for Hadron Emission Reactions With Interfering Gluons (including supersymmetric processes)", JHEP 0101 (2001) 010

[29] S. Moretti, K. Odagiri, P. Richardson, M. H. Seymour, and B. R. Webber, "Implementation of supersymmetric processes in the HERWIG event generator", JHEP 0204 (2002) 028

[30] J. M. Butterworth, J. R. Forshaw, and M. H. Seymour, "Multiparton Interactions in Photoproduction at HERA", Z. Phys C72 (1996) 637-464

[31] The CTEQ Collaboration, J. Pumplin, D.R. Stump, J. Huston, H.L. Lai, P. Nadolsky and W.K. Tung, JHEP 0207 (2002) 012, hep-ph/0201195.

[32] T.Sjostrand, S. Mrenna, P.Skands, CERN-LCGAPP-2007-04, FERMILAB-PUB-07-512-CD-T (2007)

[33] S. Frixione and B.R. Webber, JHEP 0206 (2002) 029 hep-ph/0204244

[34] S. Fixione, P. Nason, and B. R. Webber, "Matching NLO QCD and parton showers in heavy flavour production", JHEP 0308 (2003) 007

[35] ALPGEN, a generator for hard multiparton processes in hadronic collisions, M.L. Mangano, M. Moretti, F. Piccinini, R. Pittau, A. Polosa, JHEP 0307:001,2003, hep-ph/0206293.

[36] Nuclear Instruments and Methods in Physics Research A 506 (2003) 250-303

[37] IEEE Transactions on Nuclear Science 53 No. 1 (2006) 270-278

[38] Athena framework https://twiki.cern.ch/twiki/bin/view/Atlas/AthenaFramework

[39] ATLAS Physics: The Standard Model dpnc.unige.ch/cartigny2007/Hamilton_Atlas_Physics_SM.pdf

[40] Blazey, G.C. et al., Run II jet physics, Preprint hep-ex/0005012v2, 2000

[41] S. Hassini, et al., NIM A572 (2007) 77–79

[42] A study of the systematics due to parton densities and scale dependence http://arxiv.org/abs/hep-ph/0303085v1

[43] F.James, L Lyons, Y Perlin. *Workshops on Confidence Levels* CERN, Geneva 2000-005

Chapter 8

Appendix

Here, the Gaussian fits to the slices of figure 4.9 are presented. In increasing P_T left to right and down the page.

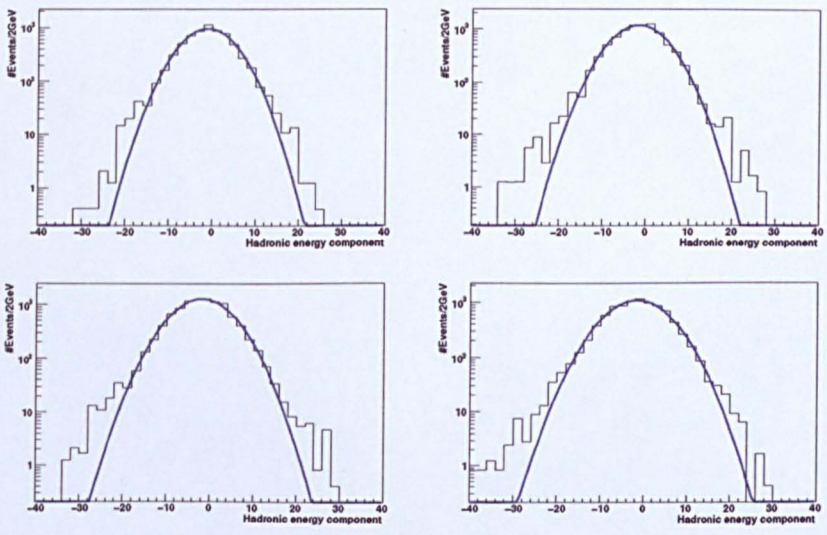

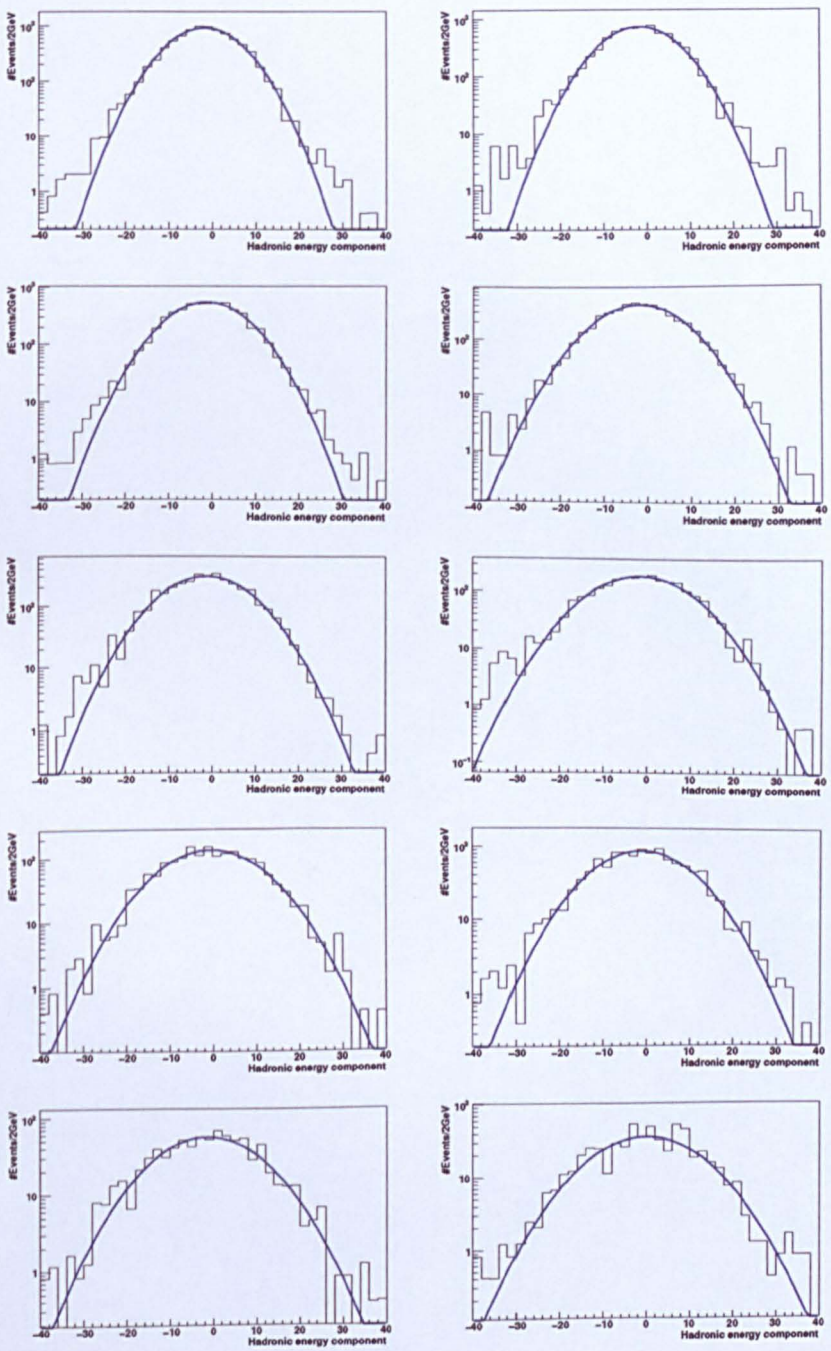
#Events/2GeV
Hadronic energy component

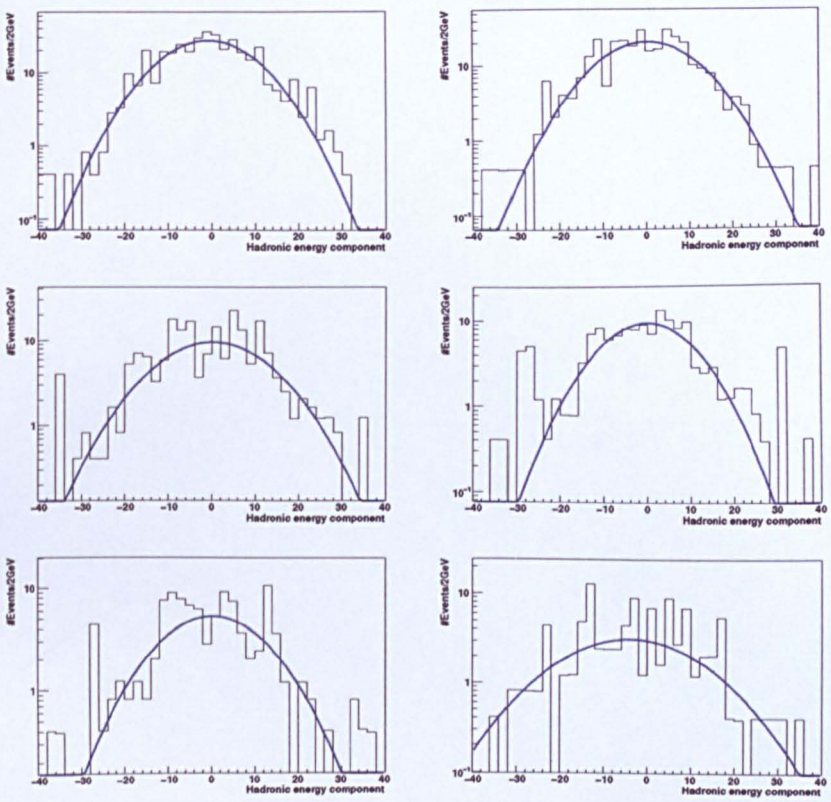
#Events/2GeV
Hadronic energy component